

# GAS AND DUST IN THE TAFFY GALAXIES: UGC 12914/15

Ming Zhu

*Joint Astronomy Centre, National Research Council Canada, 660 N. A'ohoku Place, Hilo,  
Hawaii 96720, USA*

Yu Gao

*Purple Mountain Observatory, Chinese Academy of Sciences, 2 West Beijing Road,  
Nanjing 210008, China*

E. R. Seaquist

*University of Toronto, Department of Astronomy and Astrophysics, 60 St. George Street,  
Toronto, ON, M5S 3H8, Canada*

Loretta Dunne

*Institute for Astronomy, Royal Observatory Edinburgh, Blackford Hill, Edinburgh, EH9  
3HJ, UK*

## ABSTRACT

We present a comprehensive study of the dust and gas properties in the after-head-on-collision UGC 12914/15 galaxy system using multi-transition CO data and SCUBA sub-mm continuum images at both 450 and 850 $\mu$ m. CO(3-2) line emission was detected in the disks of UGC 12914 and UGC 12915 as well as in a bridge connecting the two galaxies. Dust emission at 450 $\mu$ m was detected for the first time in the two galactic disks and in the connecting bridge. Using an LVG excitation analysis model we have obtained good estimates of the physical parameters in different regions of this system and the amount of molecular gas was found to be 3–4 times lower than that estimated by other investigators using the standard Galactic CO-to-H<sub>2</sub> conversion factor. Comparing with the dust mass derived from the SCUBA data, we found that the gas-to-dust ratio was comparable to the Galactic value in the two galaxy disks but a factor of  $\sim 3$  higher in the bridge. The physical condition of the molecular gas in the bridge is comparable to that in the diffuse clouds in our Galaxy. Our result is consistent with the scenario that the bridge molecular gas originated from the disk molecular clouds and has been drawn out of the galactic disks due to direct cloud-cloud collision.

Our data indicate that the global star formation efficiency (SFE,  $L_{IR}/M_{H_2}$  ) in UGC 12915 is comparable to that of normal spiral galaxies, and the SFE is 40% lower in UGC 12914 than in UGC 12915. Little star formation activity was found in the bridge except in an H II region adjacent to the disk of UGC 12915.

*Subject headings:* galaxies: individual (UGC 12914/15, VV 254) — galaxies: interactions — galaxies: star formation — galaxies: dust — galaxies: ISM — radio lines: galaxies

## 1. INTRODUCTION

Galaxy interactions play a crucial role in galaxy evolution, especially in the early universe where collisions and interactions are expected to be more frequent. It has been established that slow speed close collisions which lead to the merging of two galaxies could trigger intense starbursts. Gas-rich mergers could reach the phase of an ultraluminous infrared galaxy, and eventually lead to the formation of an elliptical galaxy (Sanders & Mirabel 1996). However, not all galaxy interactions will result in a merger and it is equally important to study different types of galaxy interaction to understand their role in galaxy evolution.

The Taffy galaxy pair (UGC 12914/15) represents a post collision system consisting of two counter-rotating disks with a remarkable bridge of gas and dust between them (see the background image in Fig 2). The southern galaxy, UGC 12914, contains a stellar ring which suggests that it has suffered a direct hit by the intruder, UGC 12915, at a speed much higher than the galactic rotation velocities (Struck 1999). During the “splash”, collisions between stars are unlikely, but collision between the interstellar medium (ISM) of the two disks is inevitable. Previous CO and H I observations have revealed huge amounts of atomic and molecular gas between the two galactic disks (Condon et al. 1993; Gao, Zhu & Seaquist 2003, hereafter GZS03). This gas is thought to be either dragged out from the disks, or the result of direct cancellation of the motion of the giant molecular clouds (GMCs) in the disks after the counter-rotating, interpenetrating and head-on collision. Condon et al. (1993) dubbed this system the “Taffy” galaxies when they discovered a very bright radio synchrotron bridge connecting the two spiral galaxies in the VLA 20 cm continuum map. The H I flux density peaks at the center of the bridge, and both single dish (Braine et al. 2003) and interferometer measurements (GZS03) of the CO(1–0) show that there are  $4 - 14 \times 10^9 M_\odot$  of molecular gas in the bridge region (assuming a conventional  $X$  factor), more than the total amount of that in our Galaxy. The origin of this huge amount of gas and its fate is crucial to understanding the ISM evolution and star formation in this interacting pair.

The Taffy galaxy pair is very luminous in far-infrared (FIR), with a total  $M_{H_2} = 4.5 \times 10^{10} M_\odot$  and  $L_{\text{IR}} = 8.1 \times 10^{10} L_\odot$  (GZS03), essentially qualifying as a luminous IRAS galaxy. The mid-IR (MIR) image (Jarrett et al. 1999) from the Infrared Space Observatory (ISO) shows that UGC 12915 is very bright in the MIR, suggesting vigorous star formation activity in this system. Outside the disk of UGC 12915, an H II region is clearly seen in the ISO image as well as in the  $H_\alpha$  image (Bushouse & Werner 1990), suggesting that stars are forming in the bridge. However, the global star formation efficiency (SFE),  $L_{\text{IR}}/M_{H_2}$  is  $\sim 2 L_\odot/M_\odot$  is relatively low compared to many normal spiral galaxies, and 10 times lower than that of most luminous IRAS galaxies (Gao & Solomon 1999). Why is the global SFE so low for such a strongly disturbed gas rich system? Has the mass of molecular gas been overestimated by using a standard conventional CO-to-H<sub>2</sub> conversion factor  $X$ ?

In this paper, we present a comprehensive study of the dust and molecular gas in the Taffy galaxies. We have mapped the cold dust emission at both 450 and 850 $\mu\text{m}$  using SCUBA on the James Clerk Maxwell Telescope (JCMT), which allows us to make an independent estimate of the gas mass. We have also used the JCMT to observe the CO(3–2) and CO(2–1) line emission in various regions. Combining these data with the CO(1–0) data from the BIMA interferometer (GZS03) and the CO(2–1) data from the IRAM 30m telescope (Braine et al. 2003), we have used an LVG model to constrain the physical parameters in the molecular clouds. This allows us to make a more accurate estimate of the  $X$  factor and hence a more reliable measurement of the molecular gas mass in the bridge.

We assume a Hubble constant  $H_0 = 75 \text{ km s}^{-1} \text{ Mpc}^{-1}$  throughout. The distance is assumed to be 59.3 Mpc in our calculations.

## 2. Observations and data reduction

### 2.1. SCUBA Observations

Simultaneous observations at 450 and 850 $\mu\text{m}$  using the Submillimetre Common-User Bolometer Array (SCUBA) were carried out at the JCMT on 23 Dec 2002 and 16 Sep 2004 in exceptionally good weather with CSO Tau=0.03 at 225 GHz. Two pointings were made centered on the two galaxy nuclei in order to make a mosaic image of the entire system. These two pointings provide sufficient coverage of the taffy feature between the two galaxies and the resulting best rms is in the overlap field of the mosaic. There is full coverage of the whole system including the tidal features/tails which are prominent in the H I maps and deeper optical images. The Taffy galaxies were also observed in 1998 as part of the SLUGS survey (Dunne et al. 2000). We have retrieved these data from the JCMT archive

and combined all of them to make an image at  $850\mu\text{m}$ . The  $450\mu\text{m}$  map contains only data from 2002 and 2004 because the 1998 data were taken in poorer atmospheric conditions and were therefore not useful at this wavelength. The  $450\mu\text{m}$  data are of exceptional quality and show the value of working at this wavelength when conditions allow. Uranus and CRL618 were used for flux calibration. Different flux conversion factors (FCFs) have been applied to the raw data before co-adding. Table 1 summarizes the observational details.

Pointing was checked regularly by observing the nearby blazar 2251+158 and was always better than  $3''$ , much smaller than the primary beam of the array of  $8''$  at  $450\mu\text{m}$  and  $15''$  at  $850\mu\text{m}$ . The average sky opacity in terms of CSO  $\tau$  at  $225\mu\text{m}$  during the observations is given in column 6 of Table 1.

All of the maps were made in jiggle-mode where the chop throw and direction were chosen to avoid chopping onto emission from the neighbouring galaxy. The data were reduced using the standard SURF reduction routines (Jenness & Lightfoot 1998), following the steps: flat-fielding, extinction correction using the polynomial fits to the CSO tau data, spike removal and noisy bolometer removal prior to sky subtraction. To remove the sky the task 'remsky' was used and the bolometers to estimate the sky level were chosen to avoid the region containing the galaxies and bridge (where source emission was likely to be present). The median method was chosen to remove the sky and the subtracted value not added back on. The individual sub-maps were corrected for their non-zero baselines before co-adding and the noise on each map used to determine its weight in the final co-add. The data sets were co-added and regridded using 'rebin'.

A noise map was also made using a Monte-Carlo method (described in detail in Eales et al. 2000). This allows us to account for the varying noise levels across the image, which are rather non-uniform due to data being taken on different nights and also because of noisy pixels. The sub-mm images shown in Fig. 1 are signal-noise images made from the ratio of the flux map with the noise map.

We estimate a conservative uncertainty of 15% and 30% in the derived fluxes at  $850\mu\text{m}$  and  $450\mu\text{m}$  respectively. The statistical uncertainty on the fluxes was estimated using the formula given by Dunne et al. (2000) and found to be of order 5-9% at  $450\mu\text{m}$  and  $850\mu\text{m}$ . The main source of uncertainty in the final fluxes is therefore the absolute calibration. The rms is 11.8 mJy/beam at  $450\mu\text{m}$  and 3.3 mJy/beam at  $850\mu\text{m}$  in the overlap region of the mosaic image and slightly higher in the outer regions.

## 2.2. The CO(3–2) and (2–1) Observations

Half of the  $^{12}\text{CO}$ (3–2) data were taken in one observing run during Aug 1999. The other  $^{12}\text{CO}$ (3–2), (2–1) and  $^{13}\text{CO}$ (2–1) data were taken in flexible scheduling mode at the JCMT during Aug and Oct 2003. Receiver B3 was used to observe the  $^{12}\text{CO}$  and  $^{13}\text{CO}$   $J=3-2$  transitions at 345.796 GHz, while receiver A2 was used to observe the  $^{12}\text{CO}$  and  $^{13}\text{CO}$  (2–1) transitions at 230.538 GHz and 220.399 GHz respectively. The B3 receiver has dual polarized mixers, permitting an increase in sensitivity by a factor of  $\sqrt{2}$  when observing in the dual-channel mode. The system temperatures measured were  $T_{\text{sys}} \sim 300 - 500$  K for receiver B3 and  $T_{\text{sys}} \sim 300$  K for receiver A2.

The Digital Autocorrelation Spectrometer (DAS) was employed which provides a total usable bandwidth of 920 MHz (802  $\text{km s}^{-1}$ ) for B3 and 760 MHz (980  $\text{km s}^{-1}$ ) for A2. The spectrometer band was centered at  $V_{\text{LSR}} = 4400 \text{ km s}^{-1}$ . The frequency resolution was 0.625 MHz, which corresponds to a velocity resolution of 0.545  $\text{km s}^{-1}$  at 345 GHz and 0.84  $\text{km s}^{-1}$  at 230 GHz. The beam shape of the telescope is closely approximated by a Gaussian with  $\text{HPBW}=14''$  at 345 GHz and  $20''$  at 230GHz.

All the data were taken by beam-switching in azimuth using a beam throw of  $150''$  at  $\text{PA}=90$ . Pointing was monitored frequently by observing the blazar 2251+158 and the variable star RAnd (spectral-line pointing). The rms pointing error was found to be  $\sim 2.5''$  for CO(3–2) and  $\sim 3''$  for CO(2–1). The spectral line intensity is calibrated in terms of  $T_A^*$ , *i.e.*, corrected for atmospheric transmission and losses associated with telescope efficiencies and rearward scatter. Conversion to  $T_{\text{mb}}$  was done by using the formula  $T_{\text{mb}} = T_A^*/\eta_{mb}$ , where the main beam efficiency  $\eta_{mb}$  is  $0.62 \pm 0.05$  for B3 and  $0.69 \pm 0.08$  for A2 according to the measurements of Uranus and Mars.

Measurements of the CO(3–2) spectral line of CRL618, OH231.8, NGC6334I at  $V_{\text{LSR}} = 0 \text{ km s}^{-1}$  were used to estimate a calibration uncertainty of  $\sim 10\%$  by comparing with standard spectra in the JCMT archives. Finally, we repeatedly monitored the spectral line emission of the map center throughout our runs and found excellent agreement among all the line profile measurements.

With limited telescope time, we mapped the Taffy galaxies at selected positions where the CO emission is strong enough for a quantitative study. The central region of UGC 12915 was fully sampled with  $7''$  spacing. Other points were chosen to match the IRAM data at the CO(2–1) transition. The integration time per point is typically 10–30 minutes depending on the strength of the signal.

Most of the CO(2–1) data were observed using the IRAM 30-m telescope. The observational details were described in Zhu et al. (1999). These data cover the entire system, but

with 11" spacing. We use the JCMT to re-observe the CO(2–1) line at selected positions in order to calibrate the fluxes measured from the different telescopes with different resolutions.

The JCMT software SPECX was used to reduce the spectral data and a linear baseline was removed from each spectrum. Table 2 lists the integrated intensity of CO(3–2) and the results are discussed in §3.3.

### 3. Result and Analysis

#### 3.1. Dust Emission

Figure 1 shows the 850 $\mu$ m contours overlaid on an 450 $\mu$ m color map. The sub-mm emission is mainly in the two galactic disks, but a dust bridge is clearly detected at both 450 and 850 $\mu$ m. The S/N is actually higher on the 450 $\mu$ m map, and this is due to a combination of the superb weather and the rather poor behaviour of the 850 $\mu$ m array, which contained many noisy bolometers. The lack of redundancy at 850 $\mu$ m (having on 37 pixels rather than 91 as at 450 $\mu$ m) means that some areas of the image have less data than others and these 'bad' regions often fell on the galaxy disks or bridge region. For this reason, the detailed morphology of the emission at 850 $\mu$ m is less reliable than at 450 $\mu$ m. This should be borne in mind by the reader when there appear to be differences in the positions of the peaks between the 850 $\mu$ m, 450 $\mu$ m and CO maps. In general, however, the maps from the two SCUBA wavelengths are consistent with each other.

Figure 2 presents the 450 $\mu$ m contours overlaid on a MIR 8 $\mu$ m image from the Spitzer Infrared Array Camera (IRAC). The dust emission from SCUBA is quite compact in the inner disk of UGC 12915, but rather evenly distributed between the two spiral arms and the nuclear region in UGC 12914. The cold dust seems to extend out along the both spiral arms into the ring in UGC 12914, suggesting that tidal forces have also affected the distribution of the cold dust. In the bridge, a significant fraction of the 450 and 850 $\mu$ m fluxes are associated with the H II region outside the disk of UGC 12915. Further away from the H II region, the emission seems to be associated with the ring of UGC 12914, but it is difficult to distinguish the bridge from the ring due to the low resolution of SCUBA. The H II region appears to be at the edge of the sub-mm peak at the bridge, suggesting that it might be just emerging from the dusty clouds and starting to clear away the nearby cold dust.

### 3.1.1. Comparison with hot dust

To compare with the hot dust distribution, we overlay the  $450\mu\text{m}$  contours on a mid-IR image at  $15\mu\text{m}$  from ISO (Jarrett et al. 1999, Fig. 3). The ISO image is in logarithmic scale and has been contrasted to show the low surface brightness emission. Both the Spitzer  $8\mu\text{m}$  image and the ISO  $15\mu\text{m}$  image trace the hot dust. The source of the MIR emission is thought to be polycyclic aromatic hydrocarbon (PAH) molecules or tiny carbonaceous grains heated by UV photons. The bridge is more apparent in the ISO  $15\mu\text{m}$  image, while the Spitzer image has higher resolution and better shows the features seen in optical wavelengths, i.e., the two galactic disks, the ring of UGC 12914 and the H II region outside the disk of UGC 12915.

The morphology of the cold dust distribution traced by the  $450\mu\text{m}$  and  $850\mu\text{m}$  emission is basically consistent with that of the hot dust. Table 3 lists the measured sub-mm flux densities in different regions, along with the ISO  $15\mu\text{m}$ , CO and H I fluxes (the comparison with CO and H I fluxes will be discussed in next section). The bridge contains approximately 18% of the total  $850\mu\text{m}$  flux, yet less than 2% of the  $15\mu\text{m}$  flux. The northern galaxy (UGC 12915) contains 41% and 44% of the  $850$  and  $450\mu\text{m}$  fluxes, while the UGC 12914 disk contains 41% and 36% at these two wavelengths. The flux ratio  $S_{450}/S_{850}$  is rather constant across the entire system (at least on a global scale), suggesting that the properties of the cool dust component are similar in the bridge and the two galaxies. Breaking down further to individual regions, we have measured the fluxes in a  $25''$  aperture centering at the nuclei of the two galaxies and the southern and northern MIR knots of UGC 12914 (Table 3). We can see that the flux ratio  $S_{450}/S_{850}$  in the disk of UGC 12914 is slightly lower in the northwest than the southeast, suggesting that the dust is colder in the northern disk of UGC 12914. This is consistent with the finding of Jarrett et al. (1999) based on the ISO MIR fluxes, in which they found that the MIR emission in northern UGC 12914 is weaker and redder in terms of the MIR color  $[11.4\mu\text{m}]/[15\mu\text{m}]$ . Since the MIR emission is produced by hot dust heated by young stars, it is a good tracer of star formation sites. The disk of UGC 12915 contributes 61% of the MIR flux, presumably generated by vigorous starbursts, hence the gas and dust is expected to be hotter in UGC 12915.

### 3.1.2. Comparison with Molecular and Atomic Gas Distribution

Figs 4a and 4b present the  $450$  and  $850\mu\text{m}$  contours overlaid on a CO(1-0) image from the BIMA interferometer, while Fig 5 shows the  $850\mu\text{m}$  contours overlaid on an H I image from the VLA. Gao et al. (GZS03) have made a thorough comparison between the CO and the H I, MIR and 20 cm radio continuum data. The bridge is very prominent in the H I,

CO and SCUBA 450  $\mu\text{m}$  map, but is less conspicuous in the 850  $\mu\text{m}$  map (less than  $3\sigma$  in most bridge region). At 850  $\mu\text{m}$ , the  $4\sigma$  contours looks more like a tail extended out from the H II region, rather than a bridge connecting the two disks. The width of this extension is  $\sim 16''$ , barely resolved by the  $15''$  beam. However, there appear to be some lower surface brightness structures between the two galactic disks at  $2\text{-}3\sigma$  level. We can estimate whether this is consistent with the CO(1-0) data. At the southwest end of the bridge, for example, at offset  $(-22'', -22'')$  from the nucleus of UGC 12915, the CO(1-0) integrated intensity  $I_{\text{CO}}$  is 21 Jy K km s $^{-1}$  in the BIMA map (GZS03), which is 1/8 of the peak flux in UGC 12915. If the  $S_{850}/I_{\text{CO}}$  flux ratio is constant, the dust emission should be 1/8 of the peak 850  $\mu\text{m}$  fluxes, which would be 7 mJy and therefore would yield only a  $2\sigma$  detection. These weak structures are seen at both 450 and 850  $\mu\text{m}$ , suggesting we are seeing a faint dusty bridge similar to that of the CO.

However, the peak sub-mm emission in the bridge is slightly offset from that of the CO and appears to be located between the CO and H I peaks (Fig. 4 and 5). This suggests that part of the dust may be associated with H I. A similar trend is also seen in the northern spiral arm of UGC 12914, in which some of the 850  $\mu\text{m}$  continuum appears to be associated with the strong H I emission in the bridge. The highest H I concentrations of the entire system are in the bridge (Fig. 3 in Gao et al. 2003), connecting the northwestern part of the UGC 12914 disk with the H I peak, the H II region, and the middle of the UGC 12195 disk. CO emission is essentially the lowest at the H I peak, but diffuse CO emission is abundant over this area. The molecular bridge is mostly related to UGC 12915, connecting the nuclear regions of both disks, with huge CO concentrations at the H II region. It is interesting to see that the cold dust bridge appears to be situated right between the H II regions and the H I peaks, forming a contiguous mixed bridge connecting the CO, dust, and H I peaks between the two galaxies. The shift between the dust and CO peaks is only  $7'' - 8''$  and for comparison the beam size at 850  $\mu\text{m}$  is  $15''$ . The bridge peak is not well defined, with a S/N of only 5–6. High resolution and high S/N data are needed to better define the dust bridge and confirm the shift from the CO bridge.

In general though, the dust emission at 450 and 850  $\mu\text{m}$  generally follows that of the CO, indicating that they are tracing the same component of the ISM. The spatial correlation between the dust and H I emission is weaker, suggesting that the majority of the cold dust is associated with dense molecular clouds.

Comparing the CO and sub-mm fluxes in Table 3, we can see that the flux ratio of  $S_{\text{CO}}/S_{850}$  is almost a constant across the system. There is not much difference between the two galaxy disks, and not much variation within the disk of UGC 12914. Even the bridge has a similar  $S_{\text{CO}}/S_{850}$  ratio to the disks. Given that a large fraction of the 850  $\mu\text{m}$  flux

is contamination by the CO(3-2) line (see section 3.2), this constant ratio may not seem surprising. However, we also compare the CO flux with that at 450 $\mu$ m ( $S_{CO}/S_{450}$  in Table 3), and here too the ratio is remarkably similar across the system suggesting that the dust and molecular gas are well mixed.

Braine et al. (2003) suggested that dust destruction by shocks could result in a higher CO/dust mass ratio in the bridge. Our direct flux measurements do not support this speculation. However we can estimate the CO-to-H<sub>2</sub> conversion factor  $X$  for the different regions, and thus we can check whether this lack of variation in the flux ratios extends to the derived masses of molecular gas and dust.

### 3.2. Dust Temperature and Mass

To estimate the dust temperature and mass, we need to remove the CO(3-2) contamination to the 850  $\mu$ m fluxes in the SCUBA band. Using the formula in Seaquist et al. (2004), but with the wide band filter profile from the JCMT website <sup>1</sup>, we derived that the SCUBA equivalent flux for the CO(3-2) line is  $S_{CO} = 0.53 I_{CO}$  mJy beam<sup>-1</sup> (K km/s)<sup>-1</sup>, where  $I_{CO}$  is the CO(3-2) integrated intensity in a 15" beam on the main-beam temperature scale.

Table 2 lists  $I_{CO}$  at 14" resolution and so we have converted them to 15" to compare with the SCUBA fluxes at each position. We estimate that about 30%–40% of the 850 $\mu$ m flux is from the CO(3-2) line and this factor does not vary significantly across the system (within 20% which is less than the absolute calibration uncertainty). Hence we can correct for the CO(3-2) contamination by applying a factor of 65% to the measured 850  $\mu$ m fluxes and derive the true 850  $\mu$ m fluxes free from the CO(3-2) line emission. The contribution of CO line emission to the 450 $\mu$ m fluxes has been shown to be negligible by Seaquist et al. (2004) and so no correction is made to the 450 $\mu$ m flux.

Combining the IRAS fluxes at 60 and 100 $\mu$ m from the revised IRAS BGS (Sanders et al. 2003) and the SCUBA fluxes at 450 and 850 $\mu$ m, we have derived the total dust mass by modeling the spectral energy distribution (SED). We found that the best fit for a single component model was with  $\beta = 1.4$ ,  $T_d \sim 30$  K,  $M_{dust} \sim 4.5 \times 10^7 M_\odot$ , however the fit is poor with a  $\chi^2$  of 2.2 (Fig. 6a). Dunne & Eales (2001) found that galaxies with better sampled SEDs (including more data points from ISO and/or other measurements) require a second colder dust component at around 20K. In addition, a fixed value of  $\beta = 2$  was strongly suggested by the uniformity of the  $S_{450}/S_{850}$  flux ratio. The need for two components is also

---

<sup>1</sup>[http://www.jach.hawaii.edu/JCMT/continuum/background/scuba\\_850filter.txt](http://www.jach.hawaii.edu/JCMT/continuum/background/scuba_850filter.txt)

physically sound, as galaxies always contain both hot dust in star forming regions and cold dust in quiescent regions. In reality, there will be dust at a range of temperatures depending on its environment, but two components is the simplest physically motivated model to fit to the data. Therefore, we also fit the fluxes with a two component SED using  $\beta = 2$  (Fig. 6b). The fit is improved with a  $\chi^2$  of 0.82. The formula we used is similar to that of Dunne & Eales (2001):

$$S(\lambda) = M_w B(\lambda, T_w) Q_{\text{em}}(\lambda) + M_c B(\lambda, T_c) Q_{\text{em}}(\lambda) \quad (1)$$

where  $S$  is the flux density at wavelength  $\lambda$ ,  $M_w$  and  $M_c$  are the masses of the warm and cold dust component,  $B(\lambda, T)$  is the Planck function,  $T_w$  and  $T_c$  are the warm and cold dust temperatures and  $Q_{\text{em}}$  is the wavelength-dependent emissivity of the grains which varies as  $\lambda^{-\beta}$  (here  $\beta = 2$ ) over the wavelength range considered. We have assumed a value for  $\kappa$  (the dust mass opacity coefficient (which is related to  $Q_{\text{em}}$  as  $\kappa = 4a\rho/3Q_{\text{em}}$ ) of  $0.077 \text{ m}^2 \text{ kg}^{-1}$  at  $850\mu\text{m}$ , and  $0.275 \text{ m}^2 \text{ kg}^{-1}$  at  $450\mu\text{m}$ .

Table 4 lists the results from the two-component SED fitting. The total dust mass is 45% higher than that derived from a one component model. This difference is due to the colder mean mass-weighted dust temperature which results from the two component fit and is consistent with the findings of Dunne & Eales (2001) for a larger sample of IRAS galaxies. Given that the two-component SED is a better fit to the data our discussion will use the dust mass derived from the two component model.

To derive the dust masses in the individual galaxies, we need to estimate their individual FIR fluxes. The Taffy galaxies were just resolved by IRAS at  $100\mu\text{m}$  and  $60\mu\text{m}$  in the IRAS High Resolution Image Restoration (HIRES) Atlas (Surace et al. 2004). Additionally, Zink et al. (2000) observed the northern galaxy, UGC 12915, twice at  $100\mu\text{m}$  using the Kuiper Airborn Observatory (KAO) with a resolution of  $36''$ , yielding a flux density of 9.9 and 11.6 Jy in two measurements. We adopt the average value of 10.6 Jy for UGC 12915, which is consistent with the HIRES flux when scaled to the total flux from the revised IRAS BGS (Sanders et al. 2003). The KAO observations did not detect obvious  $100\mu\text{m}$  emission at the bridge, and did not cover UGC 12914. The total  $100\mu\text{m}$  flux for the whole system is 14.1 Jy from IRAS, thus the flux from UGC 12914 should be 3.5 Jy. At  $60\mu\text{m}$ , we use the ratio given by Surace et al. (2004) for the two galaxies but scale the absolute fluxes to the total given by Sanders et al. (2003) as this is considered to be the most reliable. Table 4 lists the IRAS fluxes used. Using these data, we can fit the SED of UGC 12915 and UGC 12914 separately with a two-component model. The results are summarized in Table 4 and shown in Figs 6c & d. For comparison, we also list the mass of the molecular and atomic gas components in each region in Table 7.

The SEDs of both galaxies are dominated by the colder dust component, but the cold

dust is at a markedly higher temperature in UGC 12915 (24 K compared to 18 K in UGC 12914). This probably reflects the more intense interstellar radiation field in UGC 12915 as a result of its more vigorous star formation activity. Note, however, that despite UGC 12915 having a factor  $> 2$  greater  $L_{IR}$  and IRAS fluxes and a comparable  $850\mu\text{m}$  flux, it has a lower dust mass than UGC 12914. The reason for the difference in mass is that the dust is colder in UGC 12914, thus more dust is required to produce the same flux at  $850\mu\text{m}$ . This relative distribution of dust between the two galaxies is different from the molecular gas traced by CO (which is roughly equal in both), but consistent with the distribution of H I. UGC 12914 has 20% more H I than UGC 12915, but the total gas-to-dust ratio  $= (M_{HI} + M_{H_2})/M_{\text{dust}}$  is similar between UGC 12915 and UGC 12914 if the  $X$  factor is the same (see §3.6).

The total dust mass derived from fitting two galaxies separately is  $7.2 \times 10^7 \text{ M}_{\odot}$ , which is consistent with the value  $6.9 \times 10^7 \text{ M}_{\odot}$  from fitting the whole system. Given the additional uncertainties in breaking down the FIR fluxes on an individual basis (mostly due to the bridge), we will use the value from fitting the system as a whole,  $6.9 \times 10^7 \text{ M}_{\odot}$ , as the total dust mass.

### 3.3. The CO(3–2) Data and Ratios of the Integrated Line Intensities

CO(3–2) data have been obtained at selected regions. Figure 7 presents the CO(3–2) profiles, which were overlaid on the BIMA CO(1–0) zero-momentum color map. Figure 8 shows the CO(3–2) profiles overlaid on the BIMA CO(1–0) spectra at the three positions listed in Table 5 for excitation analysis.

The CO(3–2) emission is strong in the central region of UGC 12915 and we have fully sampled it. These profiles are consistent with that of the CO(1–0) (see GZS03) and the CO(2–1) (Braine et al. 2003). The peak velocity is blue shifted at the southeast end of the UGC 12915 disk and red-shifted at the northwest end. This is the typical kinematic feature for a rotational disk and has been discussed in details in Gao et al. (GZS03).

For UGC 12914, the quality of the IRAM CO(2–1) line data was poor at the northern disk due to unstable weather conditions, so we took only two CO(3–2) spectra using the JCMT in the southern disk where the CO emission was found to be strong enough for a quantitative study.

CO(3–2) is also clearly detected in the bridge. With a resolution of  $14''$ , the single dish CO(3–2) data reveal large amounts of excited molecular gas located outside the two galactic disks and some of them are unarguably separated from the H II region. Near the H II region, the CO(3–2) emission is even stronger than that on the disk of UGC 12914. The CO(3–2)

integrated intensity is listed in Table 2, together with the CO(3–2)/CO(1–0) line intensity ratios.

We define the ratios of integrated intensity of main-beam temperature as follows:

$$\begin{aligned} r_{21} &= I(^{12}CO(2-1))/I(^{12}CO(1-0)) \\ r_{31} &= I(^{12}CO(3-2))/I(^{12}CO(1-0)) \\ R_{10} &= I(^{12}CO(1-0))/I(^{13}CO(1-0)) \\ R_{21} &= I(^{12}CO(2-1))/I(^{13}CO(2-1)) \end{aligned}$$

The BIMA CO(1–0) map (GZS03) was made using the B,C and D configuration of the array. The shortest baseline was 6 m which is smaller than the diameter of an individual dish, thus in theory no short spacing should be missing and all the CO(1–0) flux should be recovered. In fact, the CO flux reported by Braine et al. (2003) using the IRAM 30m single dish telescope is consistent with that measured independently by GZS03 from the BIMA map. We have also double checked this by convolving the BIMA data to 22" resolution to compare with the IRAM CO(1–0) data at a variety of regions. No missing flux was found on the disks of UGC 12915 and UGC 12914, and a maximum of 30% flux is missing in the bridge region. Thus we can convolve the BIMA data to a resolution of 14" to derive the CO(3–2)/(1–0) ratio  $r_{31}$ .

Table 2 lists the derived  $r_{31}$  values. The uncertainty is mainly from CO(3–2), for which the baseline is not easy to determine because the profiles are rather broad and in some regions occupy almost the whole bandpass of the spectrometer. The total uncertainty is estimated to be within 20%. Pointing errors from both telescopes are much less than half the beam size, thus are not significant. The uncertainty is high at the offset (7", -7") and (-7", -7") due to poor baseline in the CO(3–2) data.

From Table 2, we can see that  $r_{31}$  does not vary significantly across the system. It is almost a constant of 0.3 – 0.4, except in the bridge region where the ratio is as high as 0.5 – 0.6 which could be due to missing flux in the CO(1–0) data.

Such  $r_{31}$  values are low compared to the average  $\langle r_{31} \rangle = 0.64$  in the nuclei of nearby spiral galaxies (Devereux et al. 1994) and IR-luminous galaxies (Yao et al. 2003). Radiative transfer analysis shows that  $r_{31} < 0.4$  indicates that the gas is either very cold or of low density  $n < 10^4 \text{ cm}^{-3}$ . Yao et al. (2003) show that  $r_{31}$  is correlated with the SFE. The low  $r_{31}$  in UGC 12914/15 is consistent with the low SFE in this system.

We have measured  $r_{21}$  with 11" resolution using the CO(1–0) data from BIMA and the CO(2–1) data from the IRAM 30-m. The CO(2–1) data (Braine et al. 2003) have a higher

uncertainty than the CO(3–2) data due to poor weather conditions. Also the bandwidth of the IRAM receiver at 230GHz was not wide enough to cover the broad line in some regions, resulting in poorly determined baselines. Nevertheless, the available data suggest that  $r_{21}$  also shows little fluctuation across the system. To evaluate the variation of  $r_{21}$  and  $R_{21}$  with different resolutions, we have re-observed the  $^{13}\text{CO}$ (2–1) and  $^{12}\text{CO}$  (2–1) lines with the JCMT at the three regions listed in Table 5, with a resolution of  $20''$ . We found that  $r_{21}$  and  $R_{21}$  do not change (less than 10%) at different resolutions, thus we adopt the average value as the estimate of the ratio at  $14''$ , which is listed in Table 5.

The  $R_{10}$ ,  $R_{21}$  ratios were taken from Braine et al. (2003) with a resolution of  $11''$ . We have re-examined the data and estimate that the lower limit for  $R_{21}$  is 30 at the bridge assuming a  $2\sigma$  upper limit for the  $^{13}\text{CO}$ (1–0) intensity.

It is well known that interacting galaxies have an unusually high  $^{12}\text{CO}/^{13}\text{CO}$  line intensity ratio  $R_{10}$  (Aalto et al. 1991, 1995, 1997; Casoli et al. 1991; Casoli, Dupraz & Combes 1992a, 1992b; Henkel & Mauersberger 1993; Henkel et al. 1998). In the Taffy galaxies, the high ratios of  $R_{10}$  and  $R_{21}$  were seen only in the bridge, which is similar to the case in the Antennae galaxies in which a high ratio of  $R_{21}$  was seen only in the overlap region. These extreme values can provide strong constraints on the physical parameters of the molecular clouds using an excitation analysis model.

### 3.4. Excitation Analysis

To estimate the physical parameters of the molecular gas, we have employed a large velocity gradient (LVG) model (*e.g.* Goldreich & Kwan 1974), in which it is assumed that the systematic motions rather than the local thermal velocities dominate the observed linewidths of the molecular clouds. We use this model to fit the observed line ratios in Table 5 for different combinations of  $(T_k, n(\text{H}_2), \Lambda)$ , where  $T_k$  is the kinetic temperature and  $\Lambda = Z_{\text{CO}}/(\text{d}V/\text{d}R)$ , with  $Z_{\text{CO}} = [^{12}\text{CO}/\text{H}_2]$  being the fractional abundance of  $^{12}\text{CO}$  with respect to  $\text{H}_2$  and  $\text{d}V/\text{d}R$  the velocity gradient. The optimum set of parameters is determined by minimizing  $\chi^2$ .

As outlined in Zhu et al. (2003), a grid of LVG models was searched in the parameter range of  $T_{\text{kin}} = 5 - 200$  K,  $n(\text{H}_2) = (0.1 - 10^4) \times 10^3 \text{ cm}^{-3}$ ,  $\Lambda = (0.1 - 10^2) \times 10^{-6}$  pc  $[\text{km s}^{-1}]^{-1}$ , and  $\eta = [^{12}\text{CO}/^{13}\text{CO}] = 20 - 200$ . These ranges cover all possible conditions found in the GMCs of our Galaxy as well as in external galaxies (see the discussion in Zhu et al. 2003 and Yao et al. 2003).

Three positions including the bridge, the central region of UGC 12915 and the southern

disk of UGC 12914, have been chosen for model fitting. The results are summarized in Table 6. As pointed out by Yao et al. (2003), the CO-to-H<sub>2</sub> conversion factor  $X$  can be directly derived from the LVG parameters using the formula

$$X = \frac{n(H_2)\Lambda}{Z_{co}T_{rad}} \quad (2)$$

Where  $T_{rad}$  is the radiation temperature for the <sup>12</sup>CO(1–0) line transition (Yao et al. 2003).

We found that the line ratios in all these regions can be fitted reasonably well using a single component model. It is well understood that models incorporating more data for starburst galaxies require at least two components – a prevailing optically thin, warm, diffuse component and an optically thick, cool, dense component with a smaller filling factor (e.g., Aalto et al. 1995). However, comparisons between single and double-component models yield approximately the same column density of H<sub>2</sub>, which is weighted strongly toward the prevailing diffuse component (e.g., Zhu et al. 2003). Therefore, we will use a single component model which requires less free parameters. The results for different regions are analyzed in the following sections.

### 3.4.1. The Disks of UGC 12915 and UGC 12914

The BIMA map of CO(1–0) shows that the molecular gas in the central region of UGC 12915 is distributed in a circumnuclear ring, this is concurred by higher resolution OVRO CO(1–0) data (Iono et al. 2005). The central 14" corresponds to the inner 4 Kpc which covers the majority of this ring. In the southern disk of UGC 12914 (UGC 12914S), the region for LVG modeling is on the disk  $\sim 17'' - 18''$  or 5 kpc away from the nucleus. Thus the gas properties should be comparable to that of a galaxy disk rather than a starburst nucleus.

The best fit parameters for UGC 12915 correspond to  $T_k = 15$  K,  $n(H_2) = 3.1 \times 10^3$   $cm^{-3}$ ,  $\Lambda = 4.0 \times 10^{-6}$  pc [km s<sup>-1</sup>]<sup>-1</sup> which yields  $r_{21}=0.80$ ,  $r_{31}=0.45$ ,  $R_{10}=12$ ,  $R_{21}=17$  (see Fig. 9a). Other combinations of parameters can also fit the ratios within the observational uncertainties. In general,  $\eta = 40 - 70$ ,  $T_k = 15 - 35$  K,  $n(H_2) = 800 - 10000$   $cm^{-3}$ ,  $\Lambda = 1 - 25 \times 10^{-6}$  pc [km s<sup>-1</sup>]<sup>-1</sup> can fit the ratios with  $\chi^2 < 2$ . Outside these ranges it is still possible to fit the observed line ratios, but those models would require an impossibly low CO abundance or unacceptably high velocity gradients. The range in the second line in Table 6 is our best estimate of the range of parameters with reasonable physical conditions.

The ranges of  $n(H_2)$  and  $\Lambda$  span one order of magnitude. But the column density  $N_{CO}/\Delta V = n(H_2) \Lambda$  can be constrained in a narrow range  $2.9 - 6.1 \times 10^{19}$   $cm^{-2}$  (km/s)<sup>-1</sup>.

According to formula (2), the consequence of a well confined  $N_{CO}/\Delta V$  is that the  $X$  factor can also be constrained in a narrow range  $2.2 - 6.1 \times 10^{19} (\frac{Z_{CO}}{10^{-4}}) \text{ cm}^{-2} [\text{K km s}^{-1}]^{-1}$ .  $Z_{CO}$  is generally assumed to be in the range  $10^{-5} - 10^{-4}$  (see the discussion in Zhu et al. 2003). We use the average value  $5 \times 10^{-5}$  here, bearing in mind the large uncertainty in this parameter and therefore in the derived  $X$  factor. Our results indicate that  $X$  is 2 – 6 times (assuming  $Z_{CO} = 0.5 \times 10^{-4}$ ) lower than the conventional value of  $X = 2.8 \times 10^{20} \text{ cm}^{-2} [\text{K km s}^{-1}]^{-1}$  (Bloemen et al. 1986; Strong et al. 1988), but comparable to  $X = 0.5 \times 10^{20} \text{ cm}^{-2} [\text{K km s}^{-1}]^{-1}$  estimated from the diffuse clouds in the Galaxy by Polk et al. (1988), and with that found in nearby starbursts galaxies (e.g., M82, Mao et al. 2000), interacting galaxies (Zhu et al. 2003) and IRAS luminous galaxies (Yao et al. 2003). Downes and Solomon (1998) used a model of radiative transfer through subthermally excited CO in a molecular disk to derive the gas mass in the central region of ultra-luminous galaxies, and they also found a factor of 5 less molecular gas mass than that derived from the standard  $X$  factor.

The southern disk of UGC 12914 has similar observed line ratios, except that the  $^{13}\text{CO}(2-1)$  data are unavailable. The best fit LVG parameters (Table 6) are similar to those of UGC 12915, but the average gas density appears to be lower. The  $X$  factor is in the range  $4.6 - 9.0 \times 10^{19} \text{ cm}^{-2} [\text{K km s}^{-1}]^{-1}$ , closer to the conventional value. The molecular clouds in both galaxies appear to remain cold, which could be due to a low level of star formation.

Braine et al. (2003) suggested that the molecular gas mass is over-estimated by a factor of 4 in UGC 12915, but not over-estimated in UGC 12914 (they used  $X = 2.0 \times 10^{20} \text{ cm}^{-2} [\text{K km s}^{-1}]^{-1}$ ). This is consistent with our results considering the large uncertainty in  $Z_{CO}$ . The northern disk of UGC 12914 has weaker CO emission, a lower dust temperature and less star formation activity compared to the southern disk (UGC 12914S), thus the  $X$  factor in the northern disk could be higher than that of UGC 12914S and closer to the conventional value.

### 3.4.2. The Bridge

In the bridge, the high  $R_{10}$  value puts a strong constraint on the  $[^{12}\text{CO}]/[^{13}\text{CO}]$  abundance ratio  $\eta$ . In LTE cases, assuming  $^{13}\text{CO}$  is optically thin, we have  $R_{10} = (1 - e^{-\tau})\eta/\tau$ , or  $\eta = R_{10}\tau/(1 - e^{-\tau})$ . Thus the high value for  $R_{10}$  implies either very high  $\eta$  or very low optical depth. If the molecular gas clouds are similar to GMCs in our Galaxy ( $\tau > 0.5$ ),  $\eta$  must be greater than 56 to satisfy  $R_{10} = 43$ . For a given  $R_{10}$ , a lower value of  $\eta$  means a lower optical depth of CO(1–0).

For non-LTE cases, our LVG modeling requires  $\eta > 50$  in order to fit the high  $R_{10}$  ratio of 43. For example, when  $\eta = 50$ , the best fit parameters require  $\tau_{10}=0.2 - 0.3$ , which is lower than that of most GMCs in our Galaxy or other galaxies. Only when  $\eta \geq 60$  do the model fits yield an acceptable value of  $\tau > 0.5$ . Table 6 lists the best estimates of parameters with  $\eta = 70$  (Br1 in Table 6), which yields the ratios  $r_{21}=0.88$ ,  $r_{31}=0.46$ ,  $R_{10}= 38$ ,  $R_{21}=44$ . The  $\chi^2$  contours are shown in Fig. 9(b).

Higher  $\eta$  can always fit the observed ratios equally well, for example the set of parameters Br2 in Table 6 have  $\eta = 100$ ,  $T_k = 30$  K,  $n(H_2)= 1500 \text{ cm}^{-3}$ ,  $\Lambda = 4.7 \times 10^{-6} \text{ pc} [\text{km s}^{-1}]^{-1}$ , can produce the ratios  $r_{21}$ ,  $r_{31}$ ,  $R_{10}$ ,  $R_{21} = 0.84$ , 0.46, 41, 50. Such a model does not require optically thin conditions (in this case  $\tau_{10} = 1.3$ ).

As reviewed by Wilson & Rood (1994),  $\eta$  is normally found to be in the range 40–75 in our Galaxy, with lower  $^{13}\text{CO}$  abundances found in the nuclear region of starburst galaxies (e.g., Henkel & Mauersberger 1993). There is only one report of  $\eta > 100$  in the literature, in which  $\eta = 150 \pm 27$  was found in the diffuse clouds of  $\zeta$  Ophiuchi (Sheffer et al. 1992). In the Taffy bridge, an LVG solution with a high  $\eta$  is attractive because it does not require optically thin  $^{12}\text{CO}$ , and the velocity gradient is more reasonable. The solution with  $\eta = 70$  requires  $\Lambda = 2.7 \times 10^{-6} \text{ pc} [\text{km s}^{-1}]^{-1}$ , which implies  $dV/dR = 18 \text{ km/s pc}^{-1}$  if  $Z_{CO} = 5 \times 10^{-5}$ , comparing to  $dV/dR = 10 \text{ km/s pc}^{-1}$  when  $\eta = 100$ . The velocity gradients in the molecular clouds in our Galaxy are around  $1 \text{ km/s pc}^{-1}$  (Bonnel et al. 2006; Knapp et al. 1988; Larson 1981). It is possible that  $dV/dR$  is higher in the bridge of the Taffy galaxies due to shocks and strong turbulence, but a significantly higher velocity gradient would be difficult to explain. Therefore, we could not rule out an extremely high  $\eta$  in the bridge. In §4.2, we discuss some scenarios that can reduce the  $^{13}\text{CO}$  abundance.

As listed in Table 6, we can constrain the LVG parameters in the range  $n(H_2) = (1.0 - 3.1) \times 10^3$ ,  $T_k = 20 - 50$  K,  $\Lambda = (1 - 4.7) \times 10^{-6} \text{ pc} [\text{km s}^{-1}]^{-1}$ ,  $\eta = 60 - 100$ .  $N_{CO}/\Delta V = (0.7 - 2.2) \times 10^{16} \text{ cm}^{-2} (\text{km/s})^{-1}$ . The range of  $X$  can be constrained in a narrow range,  $X = (2 - 3.6) \times 10^{19} \text{ cm}^{-2} (\text{K km/s})^{-1}$ , which is lower than that of the disks of UGC 12915 and UGC 12914, mainly due to the unusually high  $R_{10}$  and  $R_{21}$ . Besides the abundance  $\eta$ , the molecular clouds in the bridge appear to have a higher  $T_k$ , lower optical depth and higher velocity dispersion.

Comparing the Taffy bridge LVG parameters and  $X$  factor with the overlap region of the Antennae galaxies N4038/9 (Wilson et al. 2000, 2003; Zhu et al. 2003), the ISM in the Taffy bridge seems to be more diffuse, with a lower optical depth and smaller  $X$  factor. Similarly, Jarrett et al. (1999) have shown that the warm dust in the bridge is similar to that of high latitude cirrus clouds in our Galaxy. Hence the molecular clouds in the Taffy bridge could be similar to the Galactic diffuse clouds. The bulk of ISM in the overlap region

of the Antennae is between the Taffy disk ISM and the bridge diffuse clouds.

### 3.5. Molecular Gas Mass and SFE

Table 7 lists the mass of the molecular gas derived using the new  $X$  factors. From Table 6 we can see that the  $X$  factor is similar for both disks, thus we used the average  $X = 7.8 \times 10^{19} \text{ cm}^{-2} (\text{K km s}^{-1})^{-1}$ , which is 4 times lower than the conventional  $X$  factor  $X = 2.8 \times 10^{20} \text{ cm}^{-2} (\text{K km s}^{-1})^{-1}$ . As a result, the molecular gas mass is 4 times lower than that estimated by GZS03. In the bridge,  $X = 2.6 \times 10^{19} \text{ cm}^{-2} (\text{K km s}^{-1})^{-1}$  and thus  $M_{H_2}$  is reduced to 10 times less than the estimate in GZS03. For comparison we also list the dust mass, H I mass,  $L_{\text{IR}}$  and the derived ratios. The definition of the bridge region is somewhat arbitrary but to be consistent with previous studies we used a region similar to that of GZS03.

Our new result indicates that the global  $M_{H_2}/M_{HI}$  ratio is approximately 0.6, which is 4 times higher than the mean  $M_{H_2}/M_{HI}$  ratio for an optically selected sample of late-type galaxies (0.15) by Boselli et al. (2002). UGC 12915 has a  $M_{H_2}/M_{HI}$  ratio similar to UGC 12914, while in the bridge the  $M_{H_2}/M_{HI}$  ratio is a factor of 4 lower than that in the UGC 12915 disk.

The global SFE is  $5.2 \text{ L}_\odot/\text{M}_\odot$  in UGC 12915 which is similar to that of normal spiral galaxies and one order of magnitude lower than that from IR luminous galaxies in the SLUGS survey (Yao et al. 2003). This is consistent with the low  $r_{31}$  ratio found in this system. The SFE is twice as high in UGC 12915 compared to UGC 12914.

We cannot fit an SED to the bridge region as there are no resolved FIR fluxes. To estimate the dust mass in the bridge we have noted that the flux ratio  $S_{450}/S_{850}$  is very similar for the bridge and UGC 12915 and so we have assumed that the cold dust temperature is also similar. Thus we have scaled the dust mass for the bridge from that of UGC 12915 by the ratio of their  $850\mu\text{m}$  fluxes, producing a bridge dust mass of  $1 \times 10^7 \text{ M}_\odot$ . A high resolution FIR map of the system (e.g. with Spitzer or Herschel) would be required to produce a more accurate estimate of the dust masses and also the SFE for the bridge region. The global gas-to-dust ratio in the two galactic disks is consistent with that of our Galaxy, but is a factor of 2–3 higher in the bridge.

The high flux ratio  $S_{450}/S_{850}$  in the bridge (as high as that in UGC 12195) suggests that (for  $\beta = 2$ ) the dust is not colder in the bridge region despite being further from the stellar disks (which based on geometric factors should lead to a temperature about 67% of that in the disks). This is interesting in light of the very distinct properties of the bridge molecular

gas and may be related. However, given the lack of FIR data from which to constrain the temperatures, this is not yet strong evidence for a source of heating within the bridge.

### 3.6. A Gas-to-dust Ratio Map

In order to examine the variation of the gas-to-dust ratio across the system, we have convolved the CO and SCUBA 850  $\mu\text{m}$  maps to match the resolution of that of H I (18'') and combined them to derive the gas-to-dust ratio map.

The H I, H<sub>2</sub> gas mass and dust mass can be estimated by using the following formula:

$$M_{\text{HI}}(M_{\odot}) = 2.36 \times 10^5 D^2 S_{\text{HI}} \quad (3)$$

$$M_{\text{H}_2}(M_{\odot}) = 2.2 \times 10^3 D^2 S_{\text{CO}} \quad (4)$$

$$M_{\text{dust}}(M_{\odot}) = \frac{S_{850} D^2}{\kappa_{850} B_{\nu}(T_{\text{d}})} \quad (5)$$

where  $D$  is luminosity distance in Mpc,  $S_{\text{HI}}$  and  $S_{\text{CO}}$  is the H I and H<sub>2</sub> integrated flux in Jy km s<sup>-1</sup>,  $S_{850}$  is the flux at 850  $\mu\text{m}$  (after correcting for the CO(3–2) contamination),  $B_{\nu}(T_{\text{d}})$  is the Planck function, and  $\kappa_{850}$  is the dust opacity per unit dust mass which is assumed to be = 0.77 cm<sup>2</sup>g<sup>-1</sup> (c.f., James et al. 2002; Dunne et al. 2000). The dust temperature  $T_{\text{d}}$  was taken to be 21 K which is the value from fitting the SED to the total fluxes in §3.2.

To derive  $M_{\text{H}_2}$  using formula (4) we used  $X = 5.6 \times 10^{19} \text{ cm}^{-2} (\text{K km s}^{-1})^{-1}$  which is the average value from our LVG modeling. We apply a single  $X$  factor to the whole map because the division of different CO regions was not well defined and we do not want to introduce artificial variation in the map. Readers should bear in mind that the molecular gas mass could be slightly underestimated in the two disks, but overestimated in the bridge because a different scaling factor was used. However, this difference has little effect on the total gas-to-dust ratio as H I dominates the gas mass in the bridge.

After applying the proper scaling factors, the 850  $\mu\text{m}$  continuum, and the H I and H<sub>2</sub> integrated intensity maps are essentially the mass distribution of different ISM components. Using the AIPS task COMB, we first added the CO and H I map together to make a map of the total gas mass  $[M(\text{H}_2) + M(\text{HI})] \propto (2.2 \times 10^3 S_{\text{CO}} + 2.36 \times 10^5 S_{\text{HI}})$ , and then divided it by the 850  $\mu\text{m}$  continuum map. The result is a map of the gas-to-dust ratio =  $[M(\text{H}_2) + M(\text{HI})]/M_{\text{dust}}$ , which is shown in Fig 10. This map clearly shows that the gas-to-dust ratio has little change within the two disks, and in both galaxies this ratio is close to that of our Galaxy (200). However, the gas-to-dust ratio is a factor of approximately 3 times higher in the bridge. As discussed in §3.5, the  $X$  factor in the bridge is very likely to

be lower than the value used for scaling the map ( $5.6 \times 10^{19} \text{ cm}^{-2} (\text{K km s}^{-1})^{-1}$ ), hence the gas-to-dust ratio could be lower than that shown in the map.

For comparison, we have also divided the CO(1–0) map by the 850  $\mu\text{m}$  continuum to make a map of the  $M_{\text{H}_2}/M_{\text{dust}}$  ratio. Interestingly, we found little variation in the  $M_{\text{H}_2}/M_{\text{dust}}$  ratio across the whole system. This  $M_{\text{H}_2}/M_{\text{dust}}$  ratio map is not shown here because it is featureless. This suggests that the dust distribution follows the molecular gas closely, and the high total gas-to-dust ratio in the bridge is mainly due to the high H I/dust ratio.

## 4. Discussion

### 4.1. Origin of the molecular gas and dust in the bridge

The bridge region of the Taffy galaxies is remarkable in that it contains a large amount of atomic and molecular gas as well as cold dust. Our LVG modeling shows that the molecular gas is optically thin in the bridge region, and the  $X$  factor is 10 times lower than the conventional value. The  $M_{\text{H}_2}$  is reduced to  $1.3 \times 10^9 \text{ M}_\odot$ , which is only 22% of the total atomic gas mass in the same region. Thus the atomic gas is the major contributor to the gas mass of the bridge.

There are two plausible origins for the molecular gas seen in the Taffy bridge, which we will investigate in more detail below:

1. The gas originates in GMCs in the parent galaxies. The GMCs collide during the interaction and their momentum is canceled leaving them in the region between the two disks. The molecules are dissociated by shocks during the collision but are able to reform afterward.
2. The large amount of H I gas in the bridge used to be part of the diffuse phase of the ISM in the disks of the galaxies. It was removed from the disks during the collision and is now being converted into  $\text{H}_2$ .

#### 4.1.1. A GMC origin for the molecular gas

Our LVG analysis shows that the brightness dilution factor =  $\frac{T_{\text{mb}}}{T_{\text{rad}}} = \left(\frac{\Delta v}{\Delta V}\right) f_{\text{vol}}$  is  $\sim 0.02$  for the molecular clouds in both galaxy disks. The velocity filling factor  $\left(\frac{\Delta v}{\Delta V}\right)$  is  $\sim 0.1$  considering the typical velocity dispersion  $\Delta v = 20 \text{ km s}^{-1}$  in individual clouds and the FWHM line width  $\Delta V = 200 \text{ km s}^{-1}$ , thus the volume filling factor  $f_{\text{vol}}$  is 0.2. Using the

formula in section §4.3 in Braine et al. (2004), we estimate that the surface filling factor is  $\sim 0.8$ , which is much higher than the threshold value 0.2 and thus GMC-GMC collision is inevitable.

During the collision, extremely dense regions (e.g. protostars) will act as collisionless bodies like stars and will not be affected by the ram pressure. Otherwise we would expect to see more stars in the bridge, which is not the case from the Spitzer IRAC images at 3.5-5.8  $\mu\text{m}$ . The collision is most likely to occur between the diffuse low density gas surrounding the high density cores. A higher density clump will be more likely to remain in the galaxy disk as it will possess a greater momentum (which would need to be canceled in order for it to fall out of the disk). The H II region outside the disk of UGC 12915 appears to be a dense region that lost a small amount of momentum which caused it to slow down gradually and eventually drop out of the disk. Such morphology was confirmed in both the CO and sub-mm continuum map. This is not due to a gas excitation effect, but rather reflects a density gradient in the bridge that is consistent with the cloud collision scenario.

The large amount of extra-disk molecular gas (even after reduced by a factor of 8 due to the  $X$  factor) was initially a puzzle for Condon et al. (1993) because any molecules involved in collisions that are strong enough to blow a molecular cloud out of a disk would be shock destroyed in the process, and the conversion of H I to  $H_2$  is too slow under normal circumstances to have replenished the  $H_2$  outside the disks (Braine et al. 2003).

However, as pointed out by Harwit et al. (1987) and Braine et al. (2003, 2004), while GMC-GMC collisions result in complete ionization at a temperature of  $T > 10^6$  K, the cooling time for dense gas from  $10^6$  K to  $10^4$  K is less than 100 years, and  $H_2$  can form quickly in the dense post shock region. The recent theoretical work by Bergin et al. (2004) provides a more detailed picture of molecular cloud formation behind shock waves. They show that it takes  $\sim 10^6$  yr for cooling from  $10^4$  K to 25 K, and the  $H_2$  formation time scale is  $\sim 4 \times 10^6$  yr at the density of  $n = 2500 \text{ cm}^{-3}$  and  $T = 23 \text{ K}$ , which is much shorter than the age (20 Myr) of the Taffy bridge (Condon et al. 1993). Hence, as pointed out by Gao et al. (GZS03), direct GMC-GMC collision is a possible mechanism to produce large amount of molecular gas in the Taffy bridge.

This scenario is supported by the similar  $M_{H_2}/M_{\text{dust}}$  ratio across the disks and the bridge suggesting a common origin. However, the shocks which are responsible for destroying the molecules post-collision would also be expected to have an effect on the dust grains. The fact that the bridge has a normal  $M_{H_2}/M_{\text{dust}}$  ratio indicates that either the dust is not efficiently destroyed by the shocks or is able to reform *in situ* on the time-scale of 20 Myr. Dust is thought to be able to grow in the ISM by coagulation (following grain-grain collisions) or by accreting gas particles. Both processes occur more quickly in dense environments and also

require the existence of seed nuclei to begin with. Thus complete destruction of grains into the gas-phase by shocks is unlikely in this case as there is then no way for the grains to regrow on these time-scales. If the grains were sputtered or broken up into smaller fragments by the shock then is it possible that they could regrow on these time-scales? According to Whittet (2003) the time-scale for grain coagulation is given by

$$t_c = \frac{3.2 \times 10^8 \text{ yr}}{n_H v_d}$$

where  $t_c$  is the collision time-scale in yrs,  $n_H$  is the gas density in  $\text{cm}^{-3}$  and  $v_d$  is the relative velocity between grains in  $\text{km s}^{-1}$ . Using a typical value of  $v_d \sim 0.1 \text{ km s}^{-1}$  for clouds (Jura 1980) and the value of  $n_H$  from our LVG model ( $3000 \text{ cm}^{-3}$ ), we find  $t_c \sim 1 \text{ Myr}$ . This is much less than the time since the collision (20 Myr) so it is possible that dust can have re-grown in this way.

The time-scale for accretion of atoms from the gas-phase into mantles is given by Jones (2005) as  $10^9 \text{ yr}/n_H \sim 30 \text{ Myr}$  for the bridge clouds. Thus growth by accretion is not likely to be a fast enough mechanism for replenishing the dust population in the bridge.

Given that coagulation does not change the overall mass in dust, but rather changes the size distribution this does not help us recover a normal gas-to-dust ratio if there was total destruction of grains during the collisions. An investigation of the dust properties (composition and size distribution) in the bridge and disks using Spitzer IRS would provide useful constraints on the possible history of the bridge dust and thus the origin of the molecular gas.

Finally, the apparent offset between the CO, dust and H I peaks in the bridge (Figs 4 and 5) also reflects the collision scenario: if the H I peak marks roughly the point of impact, the CO and dust peaks in the bridge imply the dragging of the disk clouds of UGC 12915 from the point of impact with dense molecular gas being the most difficult to detach from the disk.

#### 4.1.2. Formation of molecular gas from the bridge H I

An alternative hypothesis is that the molecular gas is forming from the large reservoir of H I in the bridge. The conversion of H I to  $H_2$  is too slow under normal circumstances to have accounted for the  $H_2$  outside the disks (Braine et al. 2003). However, recent simulations by Glover & Mac Low (2006) suggest that  $H_2$  forms over 1-2 Myr in turbulent gas, much faster than the gravitational free-fall timescales typically required to form  $H_2$  in gravitationally

unstable, initially static gas. The large velocity gradients fitted to the bridge region would suggest a large degree of turbulence could be present and so this scenario also seems to be plausible. However, we would expect a certain degree of spatial correlation between the H I and CO distributions in this case, which is not seen in our data. Furthermore, it is difficult to explain the abnormally high gas-to-dust ratios seen in the bridge whereas a normal Galactic  $M_{H_2}/M_{\text{dust}}$ , comparable to that of both disks, is observed for the bridge molecular component. The general dust content of the atomic gas from which the  $H_2$  is purportedly forming is low compared to the disks of the galaxies,  $M_{\text{HI}}/M_{\text{dust}}$  in the bridge is 600 compared to 139 and 174 in UGC 12194/5 respectively. The dust deficient atomic gas must then somehow produce a molecular component which has a gas-to-dust ratio comparable to the clouds in the disks. This would require some fine-tuning of the atomic-molecular conversion process and so we feel it is less attractive. However, we cannot rule it out without further detailed modeling which is beyond the scope of this paper.

## 4.2. Gas properties in the bridge

Our LVG modeling indicates that the molecular properties of the bridge are similar to that of the warm, diffuse ISM in our Galaxy, with a low optical depth, low average gas density and a gas temperature higher than that of the galactic disks. The  $X$  factor is similar to that in the FIR cirrus clouds (Knapp & Bowers 1988). The  $^{12}\text{CO}/^{13}\text{CO}$  abundance ratio  $\eta$  is probably higher than that in the Galactic centre, which is also a characteristic for diffuse clouds.

There are three mechanisms that can possibly explain the high  $[^{12}\text{CO}]/[^{13}\text{CO}]$  ratio:

1) Sheffer et al. (1992) suggested that selective isotopic photo-dissociation can reduce the  $^{13}\text{CO}$  abundance in diffuse cloud. Since CO is photo-dissociated by UV radiation,  $^{13}\text{CO}$  is destroyed preferentially because  $^{12}\text{CO}$  is self-shielded to a greater extent. They reported that  $\eta = 150 \pm 27$  was observed in the warm diffuse clouds in  $\zeta$  Ophiuchi. However, there is no observational evidence for massive star formation in the bridge and so no source of UV photons to dissociate the  $^{13}\text{CO}$ .

2) Henkel & Mauersberger (1993) suggested that  $^{13}\text{CO}$  is deficient in the outer parts of galactic disks because  $^{13}\text{C}$  is produced by old stars (e.g., red giants) whereas more  $^{12}\text{CO}$  is produced by young massive stars. Regions with more massive star formation would have a higher  $^{12}\text{CO}$  abundance while the outer part of a galaxy and high latitude clouds would have less  $^{13}\text{CO}$ . If the gas from the bridge is mainly from the northern disk of UGC 12914, it would contain less  $^{13}\text{CO}$ .

3) The destruction and recombination of molecules after shocks could change the  $[^{12}\text{CO}]/[^{13}\text{CO}]$  abundance ratio. Although it is possible that  $\text{H}_2$  and  $^{12}\text{CO}$  molecules can form quickly after shocks, the formation of  $^{13}\text{CO}$  is slower than  $^{12}\text{CO}$  because it is not self-shielded and thus needs a higher gas and dust density to prevent photo-dissociation by UV radiation. Also the rare isotope molecules like  $^{13}\text{CO}$  would take longer time to form as collisions between  $^{13}\text{C}$  and dust grains are less frequent. Thus the time scale  $2 \times 10^7$  years after the collision might not be long enough for  $^{13}\text{CO}$  to reach an equilibrium abundance, and as a result the  $[^{12}\text{CO}]/[^{13}\text{CO}]$  ratio is higher than normal.

Unfortunately, detailed chemical evolution models that take account of the formation of all molecules are not available. Observationally, we can not distinguish between the above three scenarios, although we favour 2 and 3 due to the lack of an obvious source of UV photons.

If the  $[^{12}\text{CO}]/[^{13}\text{CO}]$  ratio in the bridge is indeed higher, the molecular gas would have a higher optical depth, smaller velocity gradient and a slightly higher  $X$  factor. A sample solution with  $\eta = 100$  is listed in Table 6. Nevertheless, even in the extreme case with  $\eta = 200$ , the  $X$  factor =  $3.3 \times 10^{19} \text{ cm}^{-2} [\text{K km s}^{-1}]^{-1}$  in the bridge is still less than that in the two disks and the overall gas-to-dust ratio is still higher than the Galactic value.

There are some other possible mechanisms that could affect the gas properties in the bridge. The direct  $\text{H I} - \text{H I}$  cloud collision speed could be as high as 900 km/s, since the relative speed in the counter-rotating gas disks is over 600 km/s and the transverse velocity of the collision of the two disks is nearly 700 km/s (Condon et al. 1993). Such a high speed collision will inevitably create high temperatures and associated X-ray emission. Cold dust would not easily survive in this hostile environment unless the gas condenses enough to partially shield itself from the intense hot radiation.<sup>2</sup> This could explain why the  $M_{\text{HI}}/M_{\text{dust}}$  ratio is higher than the  $M_{\text{H}_2}/M_{\text{dust}}$  ratio in the bridge, e.g., most dust related to the more diffuse  $\text{H I}$  clouds has been destroyed.

In addition, supersonic speed can induce large scale shocks as evidenced here in the expanding ring structures in the bridge where stars are forming (though at low level in the Taffy system compared to more extreme cases in classical ring galaxies such as Cartwheel). Weak ring patterns are also evident in PAHs (Fig. 2) which are part of the features mixed with the more bridge-like morphologies in CO and dust in the bridge. In short, besides the main bridge molecular features extending further from the huge CO concentration in the  $\text{H II}$  regions, part of molecular gas in the bridge could have originated from other mechanisms

---

<sup>2</sup>However, sputtering lifetimes will depend strongly on the density of the X-ray plasma and so sensitive X-ray observations with XMM or Chandra would be required to check this scenario

(e.g., rings) and have different gas properties as well.

### 4.3. Large velocity gradients

Our LVG model assumes a velocity gradient higher than that found in normal molecular clouds in our Galaxy. Assuming  $Z_{CO} = 5 \times 10^{-5}$ , which is the value observed in GMCs in our Galaxy (Blake et al. 1987), the velocity gradients are  $dV/dR = 12 \text{ km/s pc}^{-1}$  in UGC 12915 and  $10 \text{ km/s pc}^{-1}$  at the bridge according to the values of  $\Lambda$  in Table 6.

As discussed in Zhu et al. (2001, 2003) and Yao et al. (2003), the velocity gradient under the virial condition would be around  $1\text{--}2 \text{ km/s pc}^{-1}$  for a spherical cloud with a mean gas density of  $1.5 \times 10^3 \text{ cm}^{-3}$ . Thus most the clouds in our LVG models are gravitationally unbound. In star forming regions in our Galaxy, outflows can easily drive the gas velocity to  $dV/dR \sim 20 \text{ km/s pc}^{-1}$  (e.g. Moriarty-Schieven et al. 2006), and it is possible that part of the velocity gradient in UGC 12915 is associated with star formation sites. For the Taffy bridge, however, no obvious star formation is seen outside the H II region in the highly sensitive Spitzer image at  $8 \mu\text{m}$  (Fig. 2), which rules out the hypothesis of large scale inflows and outflows. Hence the velocity gradient should be from strong turbulence in the diffuse clouds.

As pointed out by Condon et al. (1993) the energy stored in the magnetic field of the bridge exceeds the turbulent energy in the gas. If there is equipartition between magnetic field and cosmic ray particle energy, then the sum of the two, which is a minimum value, may act to resupply the turbulent energy, offsetting the effects of dissipation by radiation from shocks. It is thus plausible that the inferred velocity gradients are associated, not with molecular clouds, but with transient density enhancements driven by turbulence at least partially resupplied by magnetic field and cosmic rays.

On a related point, the cosmic ray particles associated with the excess synchrotron emission originating in the bridge may have their origin partly in the shocks associated with the collision, though some fraction must also originate from a pre-existing supply in the disks. Assuming equipartition, the minimum particle and magnetic energies are each about  $4 \times 10^{55} \text{ erg}$  (Condon et al. 1993), a very small fraction (0.2%) of the total gas kinetic energy associated with the collision which is at least  $2 \times 10^{58} \text{ erg}$ . Thus the role of the fields and particles might be to “store collision energy”, acting perhaps as a long lived supply for the observed turbulence.

#### 4.4. Low SFE in the gas rich interacting pair?

Our revised global SFE is now comparable to that of normal spirals, and lower than most of starburst galaxies and IR-luminous galaxies though higher than that estimated by Gao et al. (GZS03) due to the factor of 3–4 lower molecular gas mass used here. The SFE in UGC 12915 is 40% higher than in UGC 12914. Judging from the SFE, UGC 12915 now appears to be a starburst. However, it should be noted that most of the SFE values published in the literature used the conventional  $X$  factor to estimate the molecular gas which might underestimate the SFE. Comparing with the average SFE for IRAS bright galaxies in Yao et al. (2003), in which the  $X$  factor was also derived from a LVG analysis, UGC 12915 has a much lower SFE and thus does not qualify for a starburst.

A larger discrepancy now exists in the bridge because there is not a clear indicator that best describes the local star formation rate in this region. GZS03 interpret the 20cm-to-CO ratio as a SFE indicator because the radio continuum emission has been widely used as a tracer of the recent star formation in galaxies (*e.g.*, Condon *et al.* 1996; Condon 1992). Furthermore, the tight correlation between radio continuum and CO (GZS03) serves as a good argument to suggest that the local star formation rate can be approximated by radio continuum though reduced by some large factor. Using this method GZS03 found the SFE in the bridge to be mostly comparable to that of UGC 12914. Now, with the large reduction in the molecular gas mass in the bridge and assuming that the star formation rate can still be indicated by the radio continuum emission, the resulting SFE in the bridge will be a factor of 3 higher than that of UGC 12914, which is not consistent with the MIR data. Thus, most of radio continuum emission from the bridge cannot have originated from local star formation and so cannot be used as a local star formation tracer. Condon et al. (1993) estimated that synchrotron emission from radiative electrons in the Taffy bridge has enhanced the radio continuum emission by more than 50%. If the star formation rate estimated from the radio continuum is reduced by a factor of 2-3, the new SFE in the bridge would be again comparable to that of the UGC 12914.

Since the 8  $\mu\text{m}$  is virtually optically thin, the Spitzer 8  $\mu\text{m}$  data clearly show little massive star formation in the bridge except for the H II region and along the faint ring structures of UGC 12914. However, were PAHs destroyed by shocks and intense hot X-ray radiation? Appleton et al. (2006) found abundant H<sub>2</sub> molecules in the large scale bow shocks in the intergroup medium outside the galaxies in the Stephan Quintet, and star formation is obviously on-going as evidenced by the strong H<sub>2</sub> emission and H $\alpha$  emission, yet no PAHs were detected. PAH emission is usually a good indicator of star formation in galactic disks, but it gets fainter in outer disks and may not be able to trace star formation in regions like the Taffy bridge. The star formation rate estimated from IRAC 8 $\mu\text{m}$  PAH emission may

therefore be underestimated except for the H II regions.

It should be noted that the combination of the H I and H<sub>2</sub> (even with a conversion factor  $X$  nearly ten times smaller than the conventional one as deduced here) still yields a gas surface density higher than the threshold for star formation in normal galactic disks (Martin & Kennicutt 2001). Therefore, stars could be forming in the bridge, although it is also questionable that whether the criteria for disk star formation could be applied to the special geometry like the Taffy bridge. The sensitivity constraints of the KAO far-IR observations nevertheless set an upper limit to the star formation rate in the bridge to be less than  $\sim 20\%$  of that from the disks of the galaxies. We will have to wait for Spitzer’s sensitive MIPS observations to better estimate the local star formation rate in the bridge and possibly resolve these issues.

#### 4.5. Comparison with numerical simulations

The Taffy system is particularly unique as a laboratory for testing some numerical simulations. With a nearly face-on, counter-rotating collision, the relative collision speed of HI clouds is close to 900 km s<sup>-1</sup> as the estimated transverse collision speed of the two galaxies is also about 600–700 km s<sup>-1</sup> (Condon et al. 1993). At such a high speed, the diffuse gas clouds (mainly HI) collide at highly supersonic speeds. Thus, we expect an extensive “gas splash”, and possibly other observable effects of shock heating and radiative cooling as probed by numerical simulations (Struck 1997; Barnes 2002, 2004).

A simple estimate of the amount of HI left in the taffy bridge was attempted by Gao et al. (2003). For an ideal face-on disk collision with the same counter-rotating speed, all HI clouds in two disks that have collided inelastically will be left behind after collision, canceling all systematic velocities of the HI clouds, particularly if the transverse collision velocity is much smaller than the rotation speed. When the collision speed is much higher than the rotation speed, the amount of gas that collides and gets left behind will be less, depending upon the exact area of the disk-to-disk overlap and the amount of area of the disks that has been swept owing to the counter-rotation during their close impact. The Taffy system falls between the two extreme cases as the collision speed is comparable to the counter-rotation speed. We indeed observe here that nearly half of the total HI is located between the two stellar disks whereas only less than a quarter of molecular gas is left in the taffy bridge. This is because HI clouds have a disk area filling factor which is essentially unity, an order of magnitude larger than the disk area filling factor of the molecular gas. The amount of molecular gas left behind after collision is mostly controlled by this disk area filling factor besides other factors such as the rotation and collision speeds and the disk overlap area etc.

According to Toomre & Toomre (1972), the impact parameter should be smaller than the disk radii in order to produce the ring structures, rather than the prominent tidal tails. The Taffy system has both ring structures and weak tidal features, therefore the impact parameter cannot be much smaller than the disk radii since numerical simulations show that encounters with an impact parameter larger than the galactic radii can be most effective in producing long tails and stronger gas inflow toward the nuclei. Given these considerations, most of the southeast portion of the target disk (UGC 12914) might be much less damaged. A small portion of the intruder's (UGC12915) HI disk in the northwest may have suffered less impact as well, owing to this particular impact configuration. Judging from the HI distribution in Fig. 5, we can assume that more than 1/3 of HI clouds in the target galaxy reside in the southeast disk and about 1/3 of HI gas in the intruder galaxy is located in its northwest disk. Then most of the HI in the intruder and the HI in the northwest portion of the target galaxy, totaling about half of the total HI gas of the system, could have experienced a collision, owing to the sweeping of the counter-rotating disks, with the remnants mostly left behind in the taffy bridge.

Most numerical simulations of galaxy interactions (e.g. Barnes & Hernquist 1996; Springel et al. 2005; Di Matteo et al. 2005) focused on merging systems and tidal interactions, and could not be applied to the Taffy system which is a transient event. Struck (1997) simulated the direct collisions between two gas rich disks with heating and cooling. His models show that face-on disk-disk impacts are highly dissipative, and a large amount of gas can be splashed out into the bridge between the galaxies. The splash bridge is a transient event and the gas will eventually be accreted back onto the parent galaxies. Shock heating is strong on the impact, but there is rapid expansion cooling in the bridge with a time scale of  $10^7$  yr. Virtually no star formation in the “splash” bridge was predicted by these models because the gas density is low there. All these results are qualitatively consistent with observational data, in particular the HI. However, the models of Struck (1997) could not explain the existence of a large amount of molecular gas in the Taffy bridge because large clouds are expected to be dispersed by the impact. In a more recent work, Struck and Smith (2003) modeled the starburst collisional pair NGC 7714/15 which have an optical morphology similar to that of the Taffy system. These simulations can reproduce the star formation history in the bridge as well as in the disks. Apparently, the model results depend on the assumption of the star formation law and are sensitive to the details of the interactions (Barnes 2004; Struck 2005). The Taffy system is colliding at a speed much higher than that of the NGC7714/15 pair (900 km/s vs 380 km/s) with different mass ratios and disk orientations, thus a different detailed simulation is needed to predict the fate of the bridge gas and its capability of forming stars. Exploring different numerical simulations to match the observational details is beyond the scope of this paper and will be part of our future

work.

It is also worth noting that a substantial population of luminous IR galaxies (LIRGs) with dust much cooler than the local LIRGs may exist at moderate/high redshifts (Chapman et al. 2002). There is also some indication that there may be a high redshift population of sub-mm sources with excess radio emission compared to the IR/radio correlation for local galaxies. Taffy is indeed at a rather cold dust temperature and does have excess radio continuum emission in the bridge and perhaps the conditions required to produce a taffy-type system may have occurred more often at high redshift where collisions between gas-rich systems are much more frequent.

## 5. CONCLUSIONS

We have obtained highly sensitive sub-mm maps of the Taffy system at 450 and 850  $\mu\text{m}$ . The galaxies are detected at 450  $\mu\text{m}$  for the first time, and both wavelengths show the presence of cold dust in the bridge connecting the two galaxies. CO(3–2) line emission was detected in both disks of UGC 12914 and UGC 12915 as well as in the bridge. Our conclusions are summarized as the following:

1. The CO(3–2)/(1–0) integrated intensity ratio is in the range 0.3 – 0.4 throughout the system and it shows little variation. This is consistent with rather cold dust temperature and low average gas density in the Taffy system.
2. The gas-to-dust ratio is comparable to the Galactic value in the two disks, but is a factor of  $\sim 3$  higher in the bridge. However, the CO/dust mass ratio is not higher in the bridge, and the high gas-to-dust ratio is due to the high  $M_{\text{HI}}/M_{\text{dust}}$  ratio. The  $M_{\text{HI}}/M_{\text{H}_2}$  ratio is close to unity in the two disks and a factor of 3–6 times higher in the bridge, thus the dust appears to be most closely related to the molecular component in the bridge.
3. Our LVG excitation analysis suggests that the  $X$  factor in the two galaxy disks is  $\sim 7.8 \times 10^{19} \text{ cm}^{-2} [\text{K km s}^{-1}]^{-1}$ , 3–4 times lower than the standard Galactic value, and the total amount of molecular gas in the Taffy galaxies is 3–4 times lower than previous estimates based upon the standard  $X$  factor.
4. The bridge has an extremely high  $R_{21}$  and  $R_{10}$  ( $R = I(\text{^{12}CO})/I(\text{^{13}CO})$ ) ratios, suggesting that the  $\text{^{13}CO}$  abundance might be lower than that of the two galaxy disks. The molecular gas has a low optical depth and its physical condition is comparable to that in the diffuse clouds in our Galaxy. The new estimate of the molecular gas mass is  $\sim 1.3 \times 10^9 \text{ M}_{\odot}$ . The majority of the gas in the bridge is in atomic gas phase.

5. Our result is consistent with the scenario that the large amount of molecular gas in the bridge is originated from the disk molecular clouds and is a result of momentum canceling in the GMCs due to direct GMC-GMC collisions. The physical condition of the molecular gas in the bridge is comparable to that in the diffuse clouds in our Galaxy. The gas might have been ionized by strong shocks, but has quickly cooled down and re-formed molecules. The normal CO/dust ratio in the bridge shows that grain destruction in the shocks is either not effective, or that the grains have managed to reform.

6. Little starburst is found in the Taffy system except for the intruder galaxy UGC 12915. The Spitzer 8 $\mu$ m map shows little star formation activity in the bridge except in the H II region. The global SFE is comparable to that of normal spiral galaxies.

The authors wish to thank the staff of the JCMT for their generous assistance. We also thank Tom Jarrett, Jim Condon for providing digital images. YG acknowledges the supports from NSF of China (distinguished young scholars and grant #10333060) & Chinese Academy of Sciences (hundred-talent). ERS acknowledges the support of a Discovery Grant from the Natural Sciences and Engineering Research Council of Canada.

**Figures:**

Fig. 1.— The  $850\mu\text{m}$  contours overlaid on an  $450\mu\text{m}$  signal-noise map. Contour levels start at  $2\sigma$  and increment at  $\sqrt{2}$ . Both maps have been smoothed slightly, and the circles at the lower left indicate the smoothed telescope beams ( $9.4''$  at  $450\mu\text{m}$  and  $16''$  at  $850\mu\text{m}$ ). The rms is  $3.3\text{ mJy beam}^{-1}$  and  $11.8\text{ mJy beam}^{-1}$  at  $850/450\mu\text{m}$

Fig. 2.— The  $450\mu\text{m}$  contours overlaid on a near-IR image from the Spitzer IRAC at  $8\mu\text{m}$ . The contour levels start at  $2\sigma$  and increment by  $\sqrt{2}$ . The circle at the lower left indicates the smoothed telescope beam ( $9.4''$ ). The rms is  $1\sigma = 11.8\text{ mJy}$ .

Fig. 3.— The  $450\mu\text{m}$  contours overlaid on a mid-IR image at  $15\mu\text{m}$  from the ISO (Jarrett et al. 1999). The circle at the lower left indicates the smoothed telescope beam ( $9.4''$ ).

Fig. 4.— (a) The  $450\mu\text{m}$  and (b)  $850\mu\text{m}$  contours overlaid on a CO(1–0) image from the BIMA interferometer. Contour levels start at  $2\sigma$  and increment at  $\sqrt{2}$ , and the circles at the lower left indicate the smoothed telescope beams ( $9.4''$  at  $450\mu\text{m}$  and  $16''$  at  $850\mu\text{m}$ ).

Fig. 5.— The  $850\mu\text{m}$  contours overlaid on an H I image from the VLA. Contour levels are the same as in Fig 4b.

Fig. 6.— SED fitting of the total dust emission in UGC 12914/15 using a (a) single-component model; (b) two-component model; (c) two-component model for UGC 12915; (d) two-component model for UGC 12914. The filled circles with error bars are the data points at  $25, 60, 100, 450$  and  $850\mu\text{m}$ . Note that the  $25\mu\text{m}$  point is not 'fitted' but used as an upper constraint to the temperature of the warm component.

Fig. 7.— The CO 3–2) profiles overlaid on the BIMA CO(1–0) zero-momentum color map.

Fig. 8.— The JCMT CO(3–2) profiles overlaid on the BIMA CO(1–0) profiles (from Gao et al. 2003) at the three positions listed in Table 5. The CO(1–0) data have been convolved to  $14''$  to match the resolution of the CO(3–2) data.

Fig. 9.— The  $\chi^2$  contours (in logarithm) from the LVG modeling for (a) UGC 12915 (left) at the best fit temperature  $T_K = 15\text{ K}$  with  $\eta = 60$ ; (b) the bridge (right) at the best fit temperature  $T_K = 35\text{ K}$  with  $\eta = 70$ .

Fig. 10.— A color map of the gas-to-dust ratio  $[M(H_2) + M(HI)]/M_{\text{dust}}$ . The contours are the  $850\mu\text{m}$  dust emission with levels at  $0.01, 0.014 \dots 0.056\text{ Jy/beam}$  (increment  $\sqrt{2}$ ).

Fig 1 see fig1.gif

Fig 2 see fig2.gif

Fig 3 see fig3.gif

Fig 4 see fig4a.gif and fig4b.gif

Fig 5 see fig5.gif

Fig 6.

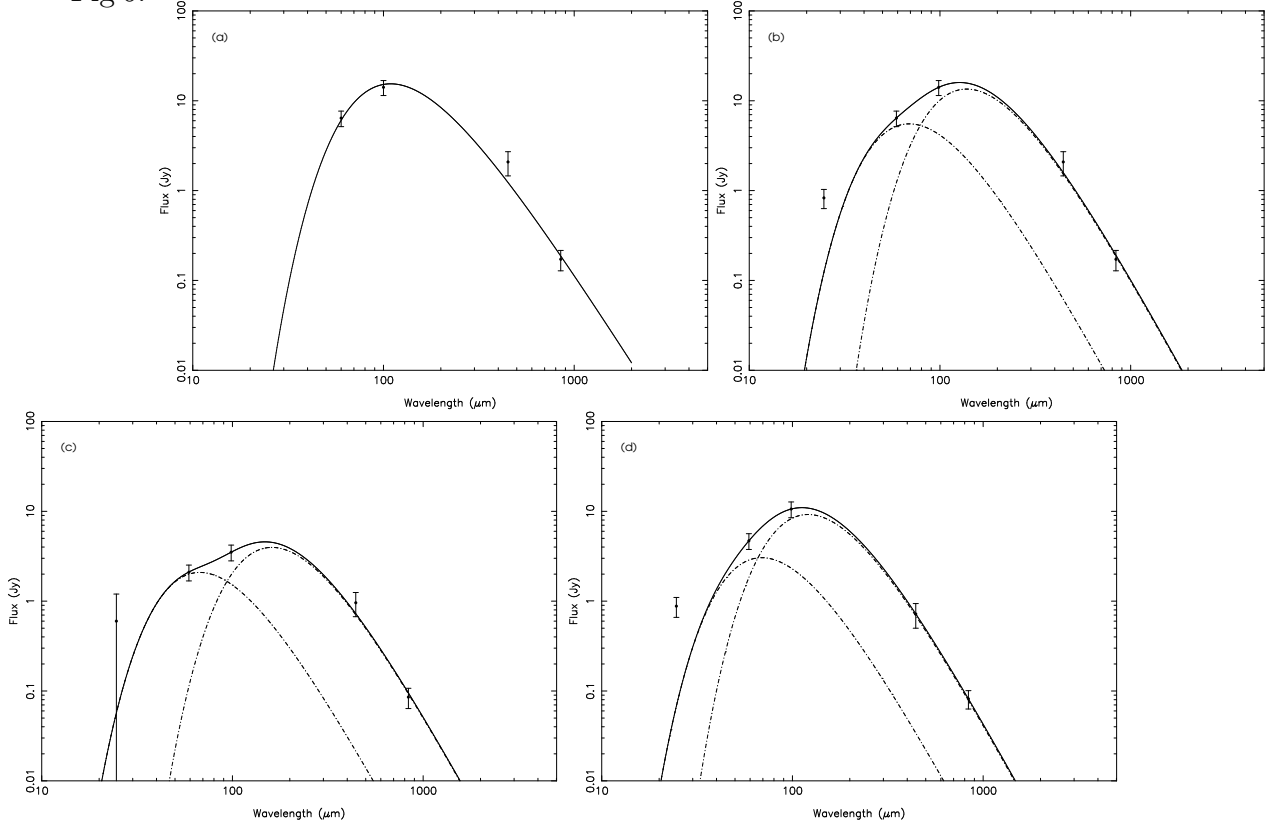


Fig 7 see fig7.gif

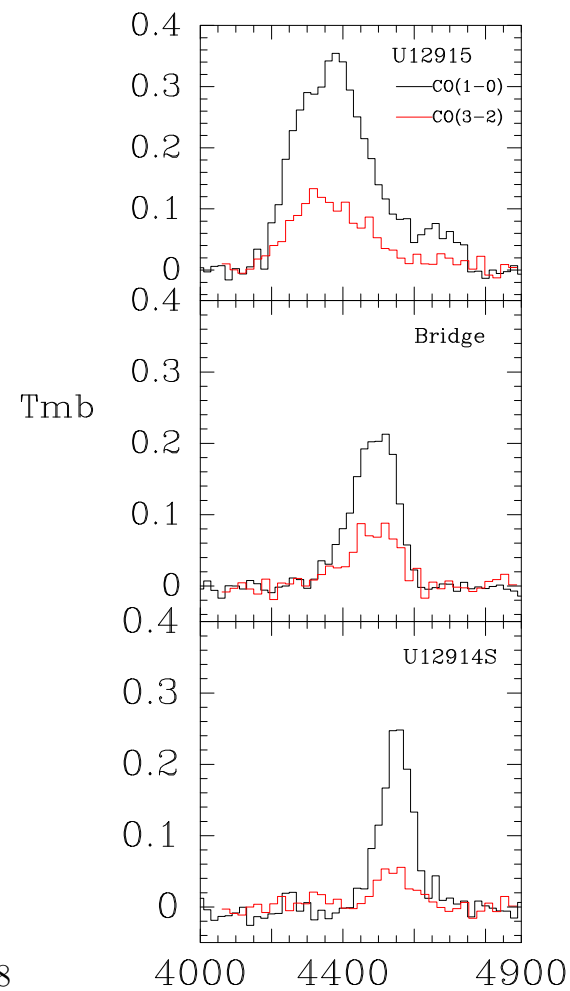


Fig 8

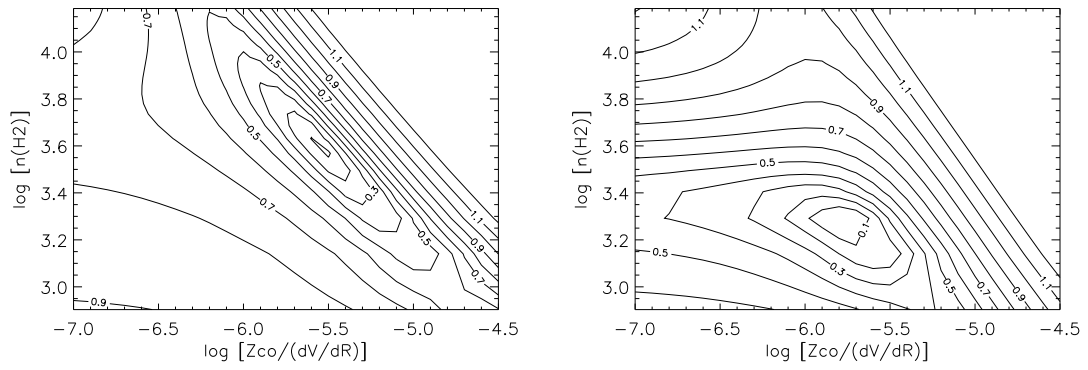
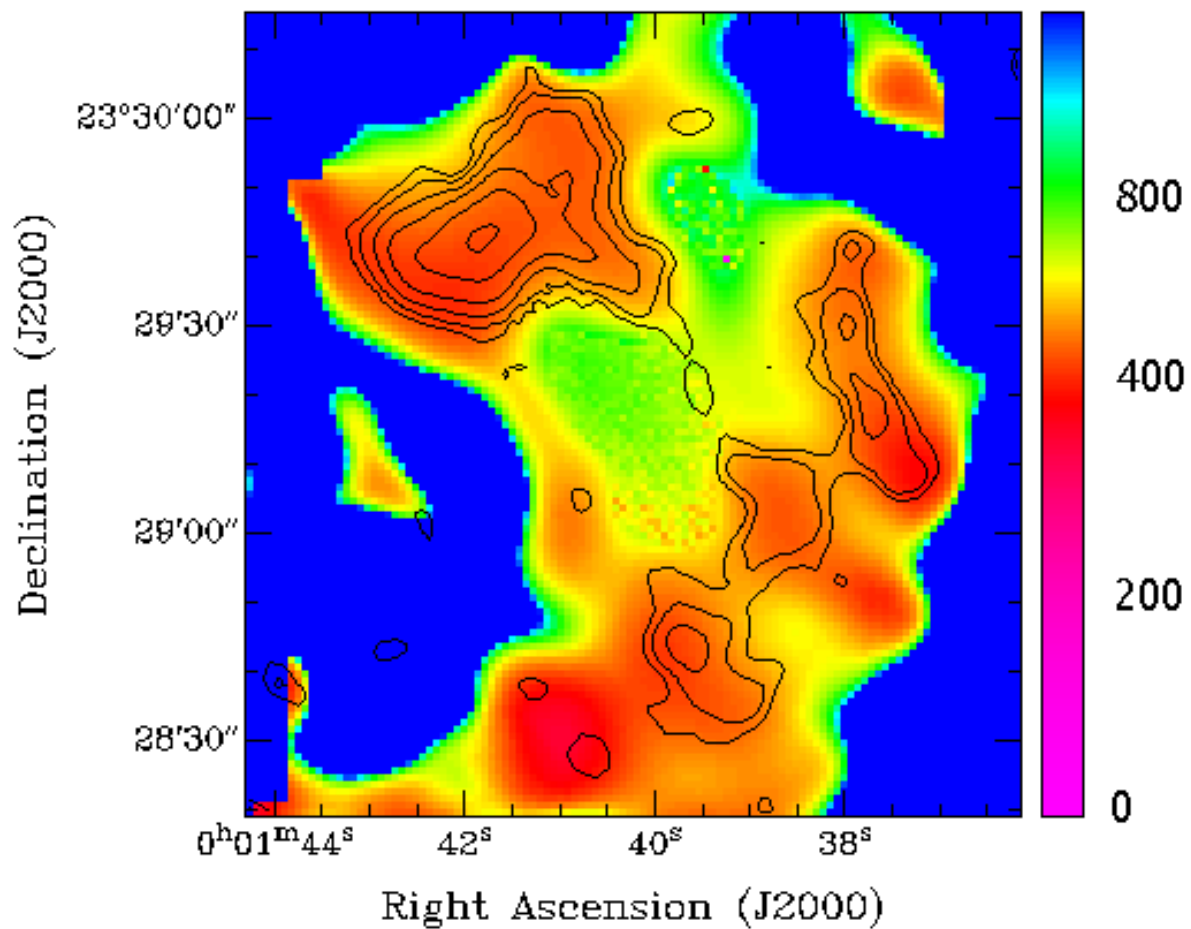


Fig 9

Fig 10



## REFERENCES

Aalto S., Black J. M., & Johansson L. E. B., & Booth R. S. 1991, A&A, 249, 323

Aalto, S., Booth, R.S., Black, J.H. & Johansson, L.E.B., 1995, A&A, 300, 369

Aalto, S., Radford, S. J. E., Scoville, N. Z. and Sargent, A. I. 1997, ApJL, 475, L107

Appleton, P. N., Xu, K. C., Reach, W., Dopita, M. A., Gao, Y., Lu, N., Popescu, C. C., Sulentic, J. W., Tuffs, R. J. & Yun, M. S. 2006, ApJ, 639, L51

Barnes, J, E. and Hernquist, L. 1996, ApJ, 471, 115

Barnes, J. E. 2002, MNRAS, 333, 481

Barnes, J. E. 2004, MNRAS, 350, 798

Bergin, E. A., Hartmann, L. W., Raymond, J. C. & Ballesteros-Paredes, J. 2004, ApJ, 612, 921

Blake, G. A., Sutton, E. C., Masson, C. R., Phillips, T. G. 1987, ApJ, 315, 621

Bloemen, J. B. G. M., Strong, A. W., Mayer-Hasselwander, H. A., Blitz, L., Cohen, R. S., Dame, T. M., Grabelsky, D. A., Thaddeus, P., Hermse, W., and Lebrun, F. 1986, A&A, 154, 25

Bonnell, I. A., Dobbs, C. L., Robitaille, T. P., Pringle, J. E. (2006) MNRAS 365, 37

Boselli, A., Lequeux, J., Gavazzi, G. 2002, A&A, 384, 33

Braine J., & Combes F., 1992, A&A, 264, 433

Braine, J., Davoust, E., Zhu, M., Lisenfeld, U., Motch, C. & Seaquist, E. R. 2003, A&A 408, L13

Braine J., Lisenfeld, U., Duc, P.-A., Brinks, E., Charmandaris, V. & Leon, S. 2004 A&A, 418, 419

Bryant P. M., & Scoville N. Z. 1996, ApJ, 457, 678

Bushouse & Wener 1990, ApJ, 359, 72

Casoli, F., Dupraz, C., Combes, F., and Kazes, I. 1991, A&A 251, 1

Casoli, F., Dupraz, C., and Combes, F. 1992a, A&A, 264, 49

Casoli, F., Dupraz, C., and Combes, F. 1992b, A&A, 264, 55

Chapman, S. C., Lewis, G. F., Scott, D, Borys, C. and Richards, E. 2002, ApJ 570, 557

Condon, J. J. 1992, ARAA, 30, 575

Condon, J.J., Helou, G., Sanders, D.B., & Soifer, B.T. 1993, AJ, 105, 1730

Condon, J.J., Helou, G., Sanders, D.B., & Soifer, B.T. 1996, ApJS, 103, 81

Devereux, N., Taniguchi, Y., Sanders, D. B., Nakai, N., & Young, J. S. 1994, AJ, 107

Di Matteo, T., Springel, V, Hernquist, L. 2005, Nature, 433, 604

Downes, D. and Solomon, P. M. 1998, ApJ, 507, 615

Dunne, L., Eales, A.S., Edmunds, M., Ivison, R., Alexander, P. & Clements, D.L., 2000, MNRAS, 315, 115

Dunne, L. & Eales, A.S., 2001, MNRAS, 327, 697

Eales, S. A., Lilly, S., Webb, T. M. A., Dunne, L., Gear, W., Clements, D. L., Yun, M. S., 2000, AJ, 120, 2244

Gao, Y., & Solomon, P. M. 1999, ApJ, 512, L99

Gao, Y., Zhu, M. & Seaquist, E. R. 2003 AJ, 126, 2171 (GZS03)

Glover, S.C.O., & Mac Low, M.-M. 2006, astro-ph/0605120/21

Goldreich, P., & Kwan, J. 1974, ApJ, 189, 441

Harwit, M., Houck, J. R., Soifer, B. T., & Palumbo, G. G. C. 1987, ApJ, 315, 28

Henkel, C. & Mauersberger, R. 1993, A&A, 274, 730

Iono, D., Yun, M.S., & Ho, P.T.P. 2005, ApJS, 158, 1

Henkel, C., Chin, Y. ., Mauersberger, R., and Whiteoak, J. B. 1998, A&A, 329, 443

James, A., Dunne, L., Ealse, S. & Edmunds, M.G. 2002, MNRAS, 335, 753

Jarrett, T.H., Helou, G., Van Buren, D., Valjavec, E., & Condon, J.J. 1999, AJ, 118, 2132

Jenness, T. & Lightfoot, J. F. 1998, in ASP Conf. Ser. 145, Astronomical Data Analysis Software and Systems VII, ed. R. Albrecht, R. N. Hook, & H. A. Bushouse (San Francisco: ASP), 216

Jones, A. P., 2005, in Proc. The Dusty and Molecular Universe: a prelude to Herschel and ALMA, ed. A. Wilson, ESA SP-577, p. 239

Jura, M., 1980, ApJ, 235, 63

Knapp & Bowers, P.F. 1988, ApJ, 331, 974

Larson 1981, MNRAS, 194, 809

Mao, R. Q., Henkel, C., Schulz, A., Zielinsky, M., Mauersberger, R., Störzer, H., Wilson, T. L., & Gensheimer, P. 2000, A&A, 358, 433.

Martin, C. L., & Kennicutt, R. C. 2001, ApJ, 555, 301

Moriarty-Schieven, G.H., Johnstone, D., Bally, J. & Jenness, T. 2006, ApJ, in press

Polk, K. S., Knapp, G. R., Stark, A. A. & Wilson, R. W. 1988 ApJ, 332, 432

Sanders, D. B. & Mirabel, I. F., 1996, ARAA, 34, 749

Sanders, D. B., Mazzarella, J. M., Kim, D.-C., Surace, J. A., Soifer, B., T., 2003, AJ, 126, 1607

Sequist, E.R., Yao, L., Dunne, L. & Cameron, H., 2004, MNRAS, 349, 1428

Sheffer, Y., Federman, S.R., Lambert, D.L. & Cardelli, J. A. 1992, ApJ, 397, 482

Springel, V. Di Matteo, T., Hernquist, L. 2005, MNRAS, 361, 776

Strong, A. W., Bloemen, J. B. G. M., Dame, T. M., Grenier, I. A., Hermsen, W., Lebrun, F., Nyman, L. ., Pollock, A. M. T., and Thaddeus, P. 1988, A&A, 207, 1

Struck, C. 1997, ApJS, 113, 269

Struck, C. 1999, Phys. Rep., 321, 1

Struck, C. and Smith B. J. 2003, ApJ, 589, 157

Struck, C. 2005, astro.ph.11335S

Surace, J. A., Sanders, D. B. & Mazzarella, J. M. 2004, AJ, 127, 3235

Toomre, A. and Toomre, J. 1972, ApJ, 178, 623

Wilson, C. D., Scoville, N., Madden, S. C., and Charmandaris, V. 2000, ApJ, 542, 120

Wilson, C. D., Scoville, N., Madden, S C. & Charmandaris, V. 2003, *ApJ*, 599, 1049

Wilson, T.L. & Rood, R.T. 1994, *ARA&A*, 32, 191

Whittet, D. C. B., 2003, *Dust in the Galactic Environment*, 2nd Ed., IoP (Bristol and Philadelphia)

Yao, L., Seaquist, E.R., Kuno, N. & Dunne, L., 2003, *ApJ*, 588, 771

Zhu, M, Seaquist, E.R., Davoust, E., Frayer, D. & Bushouse, H.A., 1999, *AJ*, 118, 145

Zhu, M., Seaquist, E. R., & Kuno, N. 2003, *ApJ*, 588, 243

Zink, E.C., Lester, D.F., Doppmann, G. & Harvey, P.M. 2000, *ApJSS* 131, 413.

**Table 1. Obs details**

| Obs. Date | Calibrator | FCF(450 $\mu$ m) <sup>a</sup> | FCF(850 $\mu$ m) <sup>a</sup> | Chop  | CSO $\tau$ | Int. Time |
|-----------|------------|-------------------------------|-------------------------------|-------|------------|-----------|
| 20040916  | Uranus     | 401                           | 285                           | 150'' | 0.030      | 2.5 Hr    |
| 20021223  | CRL618     | 263                           | 213                           | 150'' | 0.027      | 2.5 Hr    |
| 19980710  | Uranus     | 945                           | 255                           | 120'' | 0.058      | 1.2 Hr    |
| 19980421  | Uranus     | 901                           | 240                           | 120'' | 0.071      | 1.3 Hr    |

<sup>a</sup> Column 3 and 4 are the Flux conversion factor derived using the flux calibrator in column 2.

**Table 2: Integrated intensity ratios of  $^{12}\text{CO}$  J=3–2/1–0**

| $\Delta\alpha^a$<br>( $''$ ) | $\Delta\delta^a$<br>( $''$ ) | $I_{32}^b$<br>(K $\text{km s}^{-1}$ ) | $\sigma_{32}^c$<br>(K $\text{km s}^{-1}$ ) | $I_{10}^d$<br>(Jy $\text{km s}^{-1}$ ) | $r_{31}^e$ | $\sigma_{31}^f$ |
|------------------------------|------------------------------|---------------------------------------|--|--|------------|-----------------|
| 0                            | 0                            | 20.5                                  | 2  | 151                                    | 0.42       | 0.05            |
| -4.5                         | 2                            | 22                                    | 1  | 163                                    | 0.41       | 0.05            |
| -7                           | 0                            | 16                                    | 2.2  | 135                                    | 0.37       | 0.05            |
| 0                            | -7                           | 11.2                                  | 1.2  | 65                                     | 0.48       | 0.05            |
| -7                           | 14                           | 9.2                                   | 1.5  | 66                                     | 0.43       | 0.06            |
| -14                          | 14                           | 9.0                                   | 0.5  | 74                                     | 0.38       | 0.03            |
| -7                           | 7                            | 18.6                                  | 2  | 130                                    | 0.45       | 0.04            |
| 7                            | 0                            | 7.7                                   | 2.2  | 80                                     | 0.30       | 0.05            |
| 7                            | 7                            | 5.4                                   | 0.5  | 49                                     | 0.34       | 0.06            |
| 0                            | 7                            | 14.9                                  | 1  | 110                                    | 0.42       | 0.06            |
| -22                          | -22                          | 4.2                                   | 1.1  | 21                                     | 0.55       | 0.2             |
| -11                          | -11                          | 6.7                                   | 1  | 44                                     | 0.47       | 0.06            |
| 7                            | -7                           | 8.5                                   | 2.   | 48                                     | 0.54       | 0.2             |
| -7                           | -7                           | <8.0                                  | -  | 51                                     | >0.52      | -               |
| -14                          | 7                            | 9.9                                   | 1.3  | 95                                     | 0.33       | 0.1             |
| -14                          | 0                            | 9.4                                   | 1.   | 78                                     | 0.38       | 0.1             |
| -22                          | -9                           | 8.4                                   | 0.8  | 59                                     | 0.44       | 0.05            |
| -22                          | -16                          | 7.3                                   | 0.8  | 43                                     | 0.52       | 0.05            |
| U12914S                      |                              | 4.5                                   | 0.5  | 46                                     | 0.31       | 0.05            |

<sup>a</sup>  $\Delta\alpha$  and  $\Delta\delta$  are the R.A and DEC offsets from the map center R.A.=  $23^h 59^m 08.4^s$ , DEC=  $23^\circ 13' 01''$  (B1950). <sup>b</sup> The integrated intensity ( $T_{\text{mb}}$ ) of CO (3–2). <sup>c</sup> The uncertainty in  $I_{32}$ . <sup>d</sup> The integrated intensity ( $T_{\text{mb}}$ ) of CO (1–0) in a  $14''$  beam. <sup>e</sup> The ratio of  $I_{32}/I_{10}$ . <sup>f</sup> The uncertainty in the  $r_{31}$  ratio.

**Table 3: Comparison of submm fluxes with other wavelengths**

| Position <sup>a</sup> | $S_{850}$ <sup>b</sup><br>(mJy) | $S_{450}$ <sup>c</sup><br>(mJy) | $\frac{S_{450}}{S_{850}}$ | $S_{15}$ <sup>d</sup><br>(mJy) | $S_{CO}$ <sup>e</sup><br>( Jy K km s <sup>-1</sup> ) | $S_{HI}$ <sup>f</sup><br>( Jy K km s <sup>-1</sup> ) | $\frac{S_{CO}}{S_{850}}$ | $\frac{S_{CO}}{S_{450}}$ | $\frac{S_{CO}}{S_{HI}}$ |
|-----------------------|---------------------------------|---------------------------------|---------------------------|--------------------------------|--|--|--------------------------|--------------------------|-------------------------|
| U12915                | 109                             | 921                             | 8.4                       | 276                            | 355  | 5.0  | 3.3                      | 0.39                     | 71                      |
| U12914                | 108                             | 757                             | 7.0                       | 168                            | 315  | 4.9  | 2.9                      | 0.42                     | 64                      |
| Bridge                | 48                              | 406                             | 8.5                       | 8.2                            | 100  | 1.4  | 2.1                      | 0.25                     | 71                      |
| U12915C               | 77                              | 674                             | 8.8                       |                                | 213  | 1.1  | 2.8                      | 0.32                     | 194                     |
| U12914S               | 32                              | 289                             | 9.0                       |                                | 92   | 1.0  | 2.9                      | 0.32                     | 92                      |
| U12914C               | 27                              | 244                             | 9.0                       |                                | 88   | 0.90   | 3.3                      | 0.36                     | 98                      |
| U12914N               | 24                              | 201                             | 8.4                       |                                | 81   | 0.89   | 3.4                      | 0.40                     | 91                      |

<sup>a</sup> The first three rows are the global values for each galaxy and the bridge region. The remaining rows are for a 25'' region centering at the nuclei of the two galaxies (C) and the north and south MIR knots in the disk of UGC12914. <sup>b</sup> The measured 850  $\mu$ m flux density without correcting for CO(3-2) contamination. <sup>c</sup> The 450  $\mu$ m flux density. <sup>d</sup> The ISO 15  $\mu$ m flux density from Jarrett et al. (1999). <sup>e</sup> The CO(1-0) flux density from the BIMA map (GZS03). <sup>f</sup> The HI flux density from Condon et al. (1993).

**Table 4: Dust Mass from SED fitting using a two component model**

| Position            | $S_{850}$ <sup>a</sup><br>(Jy) | $S_{450}$ <sup>a</sup><br>(Jy) | $S_{100}$ <sup>b</sup><br>(Jy) | $S_{60}$ <sup>c</sup><br>(Jy) | $T_c$ <sup>d</sup><br>(K) | $M_c$ <sup>d</sup><br>( $10^7 M_\odot$ ) | $T_w$ <sup>d</sup><br>(K) | $M_w$ <sup>d</sup><br>( $10^7 M_\odot$ ) |
|---------------------|--------------------------------|--------------------------------|--------------------------------|-------------------------------|---------------------------|--|---------------------------|--|
| U12914 <sup>e</sup> | 0.085                          | 0.96                           | 3.51                           | 2.1                           | 18                        | 4.3                                      | 43                        | 0.03                                     |
| U12915 <sup>e</sup> | 0.087                          | 1.124                          | 10.6                           | 4.31                          | 24                        | 2.8                                      | 42                        | 0.056                                    |
| Total <sup>f</sup>  | 0.172                          | 2.084                          | 14.1                           | 6.4                           | 21                        | 6.8                                      | 42                        | 0.09                                     |

<sup>a</sup> The SCUBA flux density at 850 and 450  $\mu$ m. The CO(3-2) contamination has been removed from the 850  $\mu$ m fluxes. <sup>b</sup> The FIR flux density at 100  $\mu$ m. The total flux is from IRAS (Sanders et al. 2003), the flux for UGC12915 is from KAO. The flux for UGC12914 is derived by subtracting the UGC12915 flux from the total flux. <sup>c</sup> The FIR flux density at 60  $\mu$ m. The ratio of flux between the two galaxies was taken from the HIRES paper by Surace et al. (2004) but the values scaled to the total flux from Sanders et al. (2003) <sup>d</sup>  $T_c$ ,  $T_w$ ,  $M_c$  and  $M_w$  are the temperature and dust mass of the cold and warm component from the SED fitting using a two-component model (see text for details). <sup>e</sup> Note, the bridge is not resolved by IRAS and its flux will be inextricably contained in the quoted fluxes for UGC12914 and UGC12915. We will therefore allocate the submm bridge flux equally between the two galaxies also.

<sup>f</sup> The total fluxes of whole system, including the bridge and two disks. The total dust mass is derived by fitting the SED of the total fluxes.

**Table 5: Observed line ratios <sup>a</sup>**

| Position             | $r_{21}$        | $r_{31}$       | $R_{10}$     | $R_{21}$   |
|----------------------|-----------------|----------------|--------------|------------|
| U12915               | $0.75 \pm 0.1$  | $0.42 \pm 0.1$ | $14 \pm 3$   | $15 \pm 3$ |
| Bridge               | $0.79 \pm 0.15$ | $0.44 \pm 0.1$ | 43           | $> 30$     |
| U12914S <sup>b</sup> | $0.69 \pm 0.15$ | $0.30 \pm 0.1$ | $14.3 \pm 4$ | –          |

<sup>a</sup> The average line intensity ratios in a  $14''$  beam. The intensities with a higher resolution have been convolved to  $14''$ . <sup>b</sup> UGC12914S is at offset  $(-44'', -55'')$  from UGC12915 nucleus. The CO(2–1) ratios are from the average of JCMT and IRAM data with  $11''$  and  $20''$  resolutions.

**Table 6: One-component model fitting result**

| Position | $n(H_2)$<br>$10^3 \text{ cm}^{-3}$ | $T_k$<br>K | $Z_{CO}/(\text{dV/dR})$<br>$10^{-6} \text{ pc (km/s)}^{-1}$ | $N_{CO}/\Delta V$<br>$10^{16} \text{ cm}^{-2} (\text{km/s})^{-1}$ | $\tau_{10}$ | $X$<br>$10^{19}$ | $[\frac{^{12}CO}{^{13}CO}]$ | $\chi^2$ |
|----------|------------------------------------|------------|---|---|-------------|------------------|-----------------------------|----------|
| U12915   | 3.1                                | 15         | 4.0   | 3.89  | 3.5         | 7.8              | 60                          | 1.3      |
|          | 0.8–10                             | 10–40      | 1–25  | 3–6   | 1.8–5.1     | 4.4–12.2         | 40–70                       | <2       |
| Br1      | 1.5                                | 35         | 2.7   | 1.25  | 0.7         | 2.6              | 70                          | 1.2      |
| Br2      | 1.5                                | 30         | 4.7   | 2.17  | 1.3         | 3.6              | 100                         | 0.7      |
|          | 1–3.1                              | 20–50      | 1–4.7   | 0.7–2.2   | 0.4–1.3     | 2.0–3.6          | 60–100                      | <2       |
| U12914S  | 1                                  | 15         | 12.7  | 3.9   | 5.1         | 9.0              | 70                          | 0.6      |
|          | 0.5–2.5                            | 10–45      | 4.7–19  | 2.6–4.5   | 2.3–4.1     | 4.6–10.0         | 40–70                       | <2       |

Columns 2–4 contain the LVG parameters noted above, column 5 contains the CO column density, column 6 the optical depth at the J=1–0 transition; column 7 contains the  $X$  factor in the unit of  $\text{cm}^{-2} (\text{K km s}^{-1})^{-1}$ , assuming  $Z_{CO} = 0.5 \times 10^{-4}$ . column 8 contains the assumed isotope abundance ratio, and column 9 shows the value of  $\chi^2$  associated with the fit. Note: for each position, the first row is the best fit parameters and the second row is the estimated range within the observed uncertainty.

**Table 7: Masses of different components, FIR luminosity and their ratios**

| Position | $F_{CO}$ <sup>a</sup><br>Jy Km s <sup>-1</sup> | $M(H_2)$ <sup>b</sup><br>$10^9 M_\odot$ | $M_{dust}$ <sup>c</sup><br>$10^7 M_\odot$ | $M_{HI}$ <sup>d</sup><br>$10^9 M_\odot$ | $L_{IR}$ <sup>e</sup><br>$10^{10} L_\odot$ | $\frac{M_{H_2} + M_{HI}}{M_{Dust}}$ | $L_{IR}/M_{H_2}$<br>$L_\odot/M_\odot$ |
|----------|--|---|---|---|--|-------------------------------------|---------------------------------------|
| U12915   | 355  | 4.2                                     | 2.3                                       | 4                                       | 3.6  | 356                                 | 8.6                                   |
| U12914   | 315  | 4.2                                     | 3.6                                       | 5                                       | 1.4  | 255                                 | 3.4                                   |
| Bridge   | 325  | 1.3                                     | 1.0                                       | 6                                       |  | 730                                 |                                       |
| Total    | 995  | 9.7                                     | 6.9                                       | 15                                      | 5  | 358                                 | 5.2                                   |

<sup>a</sup> The CO(1–0) flux from Table 1 of GZS03.

<sup>b</sup> The molecular gas mass derived using from the  $X$  factor in Table 6.

<sup>c</sup> The dust mass estimated by fitting the SED for each region separately. In this case the submillimetre fluxes for UGC 12914 and 12915 do not include the bridge region. However, the bridge is not resolved in the FIR and so an SED fit is not possible. The dust mass for the bridge was estimated assuming the cold temperature is similar to that in UGC 12915 (see text for details).

<sup>d</sup> The atomic gas mass derived from the HI VLA map (GZS03).

<sup>e</sup> The FIR luminosity from IRAS and KAO (Zink et al. 2000), see text for details

This figure "fig1.gif" is available in "gif" format from:

<http://arxiv.org/ps/astro-ph/0703200v1>

This figure "fig2.gif" is available in "gif" format from:

<http://arxiv.org/ps/astro-ph/0703200v1>

This figure "fig3.gif" is available in "gif" format from:

<http://arxiv.org/ps/astro-ph/0703200v1>

This figure "fig4a.gif" is available in "gif" format from:

<http://arxiv.org/ps/astro-ph/0703200v1>

This figure "fig4b.gif" is available in "gif" format from:

<http://arxiv.org/ps/astro-ph/0703200v1>

This figure "fig5.gif" is available in "gif" format from:

<http://arxiv.org/ps/astro-ph/0703200v1>

This figure "fig7.gif" is available in "gif" format from:

<http://arxiv.org/ps/astro-ph/0703200v1>